Ion-induced nanopatterns on semiconductor surfaces investigated by grazing incidence x-ray scattering techniques

D Carbone[1], **A Biermanns**[2], **B Ziberi**[3], **F Frost**[3], **O Plantevin**[4], **U Pietsch**[2] and **T H Metzger**[1]

[1] ID01, ESRF, 6 rue Jules Horowitz, F-38043 Grenoble Cedex, France
[2] Festkörperphysik, Universität Siegen, D-57068 Siegen, Germany
[3] Leibniz-Institut für Oberflächenmodifizierung e.V., D-04318 Leipzig, Germany
[4] Université Paris-Sud, Centre de Spectrométrie Nucléaire et de Spectrométrie de Masse,
UMR 8609, F-91405 Orsay, France

E-mail: gcarbone@esrf.fr

Abstract

In this review we cover and describe the application of grazing incidence x-ray scattering techniques to study and characterize nanopattern formation on semiconductor surfaces by ion beam erosion under various conditions. It is demonstrated that x-rays under grazing incidence are especially well suited to characterize (sub)surface structures on the nanoscale with high spatial and statistical accuracy. The corresponding theory and data evaluation is described in the distorted wave Born approximation. Both *ex situ* and *in situ* studies are presented, performed with the use of a specially designed sputtering chamber which allows us to follow the temporal evolution of the nanostructure formation. Corresponding results show a general stabilization of the ordering wavelength and the extension of the ordering as a function of the ion energy and fluence as predicted by theory. The *in situ* measurements are especially suited to study the early stages of pattern formation, which in some cases reveal a transition from dot to ripple formation. For the case of medium energy ions crystalline ripples are formed buried under a semi-amorphous thick layer with a ripple structure at the surface being conformal with the crystalline/amorphous interface. Here, the x-ray techniques are especially advantageous since they are non-destructive and bulk-sensitive by their very nature. In addition, the GI x-ray techniques described in this review are a unique tool to study the evolving strain, a topic which remains to be explored both experimentally and theoretically.

(Some figures in this article are in colour only in the electronic version)

1. Introduction

The evolution of surface morphology during ion beam sputtering, IBS, has received increasing attention recently [1–3]. Patterning and texturing on a nanometer length scale of metal and semiconductor surfaces has become a topic of intense research [4, 5]. One of the first periodic surface ripple structures induced by irradiation with low energy ions at oblique incidence was already observed in 1962 on SiO_2 surfaces [6]. In the following years this self-organization effect was exploited for the surface structuring of different materials such as Si, InP, GaAs, HOPG and metals [7–11]. The observed patterns and the experimental conditions to obtain them are very different in the case of semiconductors and metals. Here we focus on the results obtained by ion erosion on semiconductor surfaces.

It is well known that the surface morphology during ion erosion depends strongly on the experimental parameters:

substrate material, energy nature and incidence angle of impinging ions, substrate temperature and erosion time. Most interestingly, different combinations of these parameters give rise to very diverse surface morphologies [12]. Detailed studies on the ion-induced ripple formation on Si have revealed that they appear in a range of incident angles between 30° and 60° [10, 11] using O^2 ions in the energy range 1–9 keV. The ripple wavelength appears to be linearly dependent on the ion energy and varies in the range of 100–400 nm when the ion energy changes from 1 to 9 keV. On the other side, at low ion energies (500–2000 eV, Ar, Kr, Xe) ripple formation has been found only for incidence angles from 5° to 30° with wavelengths well below 100 nm. At higher incidence angle, instead, the surface is smoothed [13]. These results are only in apparent contrast with each other, as they are the outcome of different combinations of IBS parameters (different ions and ion energies in different ranges of incident angles). Although exponential dependences of the ripple wavelength on ion fluence, i.e. sputtering time, have been observed on different material, studies on Si surfaces at low temperatures of 100–300 K showed no temperature dependence [14]. Finally, studies at elevated temperatures of 500–750 °C with Ar^+ ions at energies from 250 to 1200 eV showed the rotation of the ripple pattern with ion fluence: at short sputtering times parallel ripples are observed, whereas at longer sputtering times the pattern evolves into perpendicular ripples with a transition regime between these two morphologies [15]. Under normal incidence, or equivalently at off-normal incidence with simultaneous sample rotation, the surface morphology evolves no longer as a periodic ripple pattern but as a hexagonally ordered pattern of mounds [16–19].

In recent times IBS has been extended to medium energy ions >10 keV. Since the end of range distance of ions is in the range of a few 10–100 nm a sharp transition from amorphous to crystalline state has been observed. As an example, a one-dimensional ripple formation on Si(100) surfaces has been observed after ion beam impact of about 10^{17} Ar^+ ions cm^{-2} with energy between 50 and 100 keV. This ripple formation takes place in a small range of incidence angles with respect to the surface normal close to 60° only. Depending on ion species (Ar^+ or Xe^+) and ion fluence the interface between amorphous to crystalline structure shows the same morphology as found at the surface. This interface morphology seems to be dependent on crystal orientation with respect to the direction of the ion beam.

A theoretical model which describes successfully the formation of ripple and mound patterns was given first by Bradley and Harper [20]. Their continuum equation (BH equation) approach, which is based on the sputter theory by Sigmund [21], and their nonlinear extension (Kuramoto–Sivashinsky-model) [22, 23] are able to describe the surface morphology after IBS as a function of ion fluence and particularly accounts for the change in ripple orientation with angle of incidence. However, the model does not include the anisotropy of the crystal lattice underneath the sputtered surface region.

Generally, characterization of samples modified by IBS is limited to the sample surface. Here, direct imaging techniques, such as atomic force microscopy (AFM), transmission electron microscopy (TEM) or scanning electron microscopy (SEM), are used to determine shape and lateral ordering of surface nanostructures. In limited cases, cross-sectional TEM measurements are used to gather the transition region between the amorphous surface region and the following crystalline host structure. These measurements are restricted to a small sample area in the range of a few nanometers and can only be performed *ex situ*, after the ion erosion process. Recent achievements in IBS have shown that understanding of ripple formation at medium energy ions requires analysis of the subsurface region too. In this respect x-ray scattering methods are powerful tools for the structural characterization, with high spatial resolution and excellent statistical accuracy. The advantage of x-ray methods, i.e. at small incidence and exit angles (grazing Incidence techniques, GI), results from the fact that the x-ray beam can be tuned to be extremely sensitive to both the surface and the subsurface regions. Because the refraction index of x-rays in matter is slightly smaller than unity an x-ray beam undergoes total external reflection at the air–sample interface which can limit the penetration depth to a few nanometers only, and probes just the range affected by IBS. The second advantage consists in the possibility to perform x-ray scattering *in situ*, during IBS erosion. To this end a sputter chamber, equipped with ion guns up to 3 keV, is installed on an x-ray diffractometer and the evolution of surface nanostructures during IBS can be studied with a time resolution of a few seconds. Major methodical developments of x-ray methods for characterization of IBS-treated samples have been performed at the ID1 beamline at ESRF. Techniques such as grazing incidence small-angle scattering (GISAXS) and grazing incidence diffraction (GID) have been successfully applied for the characterization of IBS nanostructures created by low and medium energy IBS. Whereas the latter samples have to be measured *ex situ*, low energy IBS could be observed *in situ*. In this review we will describe the basics of the grazing Incidence x-ray scattering techniques used and review various examples of *ex situ* and *in situ* sample characterization during IBS on semiconductor surfaces.

This review is organized as follows: the basics of the GISAXS and GID techniques are illustrated in section 2. Here, the typical geometry of scattering and the set-up used to perform such measurements on IBS nanopatterned surfaces are shown, both for *ex situ* and *in situ* measurements. The vacuum chamber constructed for *in situ* studies will also be described. In section 3 we will discuss the approach taken to analyze GISAXS and GID measurements performed on nanopatterned surfaces. In particular, we will introduce the models used to interpret and fit the measured data. In sections 4 and 5 results from published and on-going works are separated according to *ex situ* and *in situ* measurements as well as with respect to the ion beam energy used for the IBS process, respectively. An outlook for future work is given in section 6.

2. Technique

X-ray diffraction (XRD) is a technique largely used in condensed matter physics for structural investigations at

length scales ranging from atomic distances to sub-micron scale. Recently, with the progress of nanoscience and nanotechnology, its use has been successfully extended to study nanostructures on substrates for the determination of morphology, crystal structure, ordering and chemical composition. The GI scattering geometry is well suited for these tasks, as it permits us to overcome the weak scattering signal due to the small amount of investigated material. This scattering technique enhances the signal from surface layers while suppressing, at the same time, the strong scattering signal from the substrate. This surface sensitivity is based on the fact that the index of refraction of x-rays for condensed matter is smaller than one, cf equation (1). Thus a critical angle for total external reflection exists, equation (3):

$$n = 1 - \delta + i\beta \tag{1}$$

$$\delta = \lambda^2 \frac{r_0 N_a \rho_m}{2\pi A}(f_0 + f'); \qquad \beta = \lambda^2 \frac{r_0 N_a \rho_m}{2\pi A} f'' = \frac{\lambda \mu}{4\pi} \tag{2}$$

$$\alpha_c = \sqrt{2\delta} = \frac{\sqrt{4\pi \rho_e r_0}}{k} \tag{3}$$

where λ is the wavelength of the x-rays, N_a is Avogadro's number, $r_0 = 2.818 \times 10^{-5}$ Å is the classical electron radius, $\rho_{m,e}$ are mass and electron density, respectively, and A is the molar atomic mass. f_0, f', f'' and μ are the atomic scattering factor, the real and imaginary part of its dispersion correction and the linear absorption coefficient. For x-rays impinging at angles below this critical angle, an evanescent wave is created below the surface and propagates parallel to it. Its amplitude is maximum at the surface and is attenuated exponentially towards the bulk, with a typical $1/e$ penetration depth of some tens of nanometers, depending on the incident angle and the energy of the x-ray beam [24].

Figure 1(a) shows how the scattering depth varies as a function of the incident angle at three different values of the exit angle α_f. For α_i below the critical angle the probed depth can be of the order of 10 Å, then it rapidly increases across the critical angle up to several thousands Å, depending on the actual value of α_f, the absorption by the material and the x-ray energy. The remarkable fact is that, adjusting the value of the angles $\alpha_{i,f}$ in an appropriate way allows a fine tuning of the probed depth to achieve a depth resolution of a few Å.

The transmission coefficient T [25] of the x-rays at small angles is determined by the material's refraction index n (see figure 1(b)). In particular, the transmission coefficient is highest at the critical angle ($T = 4$ with no absorption), which means that the scattering signal from the surface is maximized when $\alpha_{i,f} = \alpha_c$ (cf figure 1(b)). Consequently, the intensity of the scattering from the surfaces layers is enhanced with respect to the bulk part.

In this section we describe the basics of the GI techniques used for the works discussed throughout the paper. GISAXS is well suited to study the shape, size and ordering of nanostructures. GID measurements, on the other hand, are sensitive to the atomic structure and thus to the crystalline core of the nano-objects. The combination of these two techniques allows one to determine all important structural properties of nanoassemblies, i.e. morphology and strain distribution in the
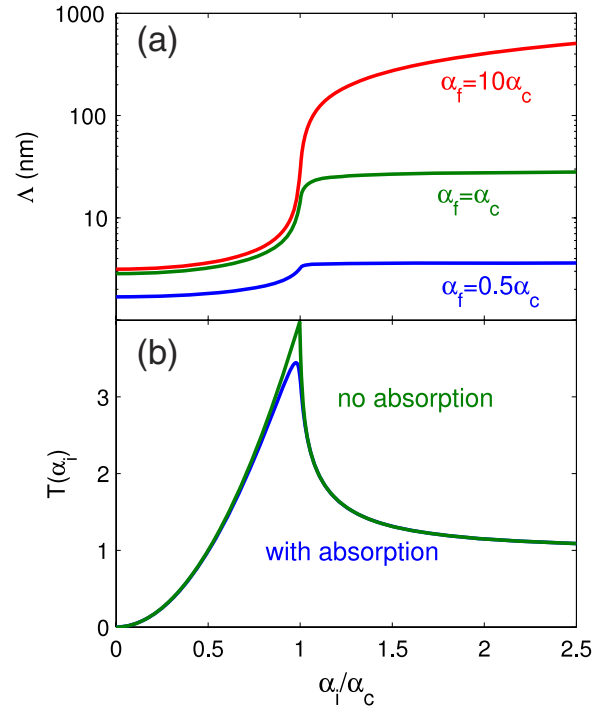

Figure 1. (a) X-ray penetration depth and (b) x-ray transmission coefficient as a function of $\alpha_{i,f}$. Values calculated for a silicon substrate and an x-ray energy of 8 keV.

nanopatterns and the underlying bulk. A schematic of the GISAXS/GID geometry of scattering is shown in figure 2. The incident x-ray beam, with wavevector $\vec{\kappa}_i$, impinges on the surface at a glancing angle α_i, close to the material's critical angle α_c. The out-coming x-ray beam with the wavevector $\vec{\kappa}_f$ is scattered under the angle 2θ. It is collected by a linear position detector or a CCD in a direction forming an exit angle α_f with respect to the surface plane and an in-plane angle 2θ with respect to the forward direction, creating a momentum transfer $\vec{q} = \vec{\kappa}_f - \vec{\kappa}_i$. The momentum transfer measured in GI geometry is often decomposed in a component parallel $\vec{q}_\parallel$ and perpendicular $\vec{q}_\perp$ to the surface: $\vec{q} = \vec{q}_\parallel + \vec{q}_\perp$. At a given energy the value of $\vec{q}_\parallel$ is determined by the scattering angle 2θ, which corresponds to the position of the detector. The angles $\alpha_{i,f}$ determine the perpendicular component and, therefore, the scattering depth Λ, that is, the extension of the probed volume below the surface:

$$\Lambda = \frac{1}{\text{Im}(q'_\perp)} = \frac{\lambda}{4\pi (B_i + B_f)} \tag{4}$$

where $q'_\perp$ is the vertical momentum transfer inside the material and

$$B_{i,f} = 2^{-1/2}\{(2\delta - \sin^2 \alpha_{i,f}) - [(\sin^2 \alpha_{i,f} - 2\delta)^2 + 4\beta^2]^{1/2}\}^{1/2}.$$

As for both, GISAXS and GID geometries, the value of $\alpha_{i,f}$ is small, $\vec{q} \approx \vec{q}_\parallel$ holds, i.e. the probed momentum transfer lies in the surface plane.

In the GISAXS geometry, the angle 2θ is also 'small' (of the order of a few m deg up to a few degrees) and the momentum transfer $\vec{q}$ is nearly perpendicular to the incoming
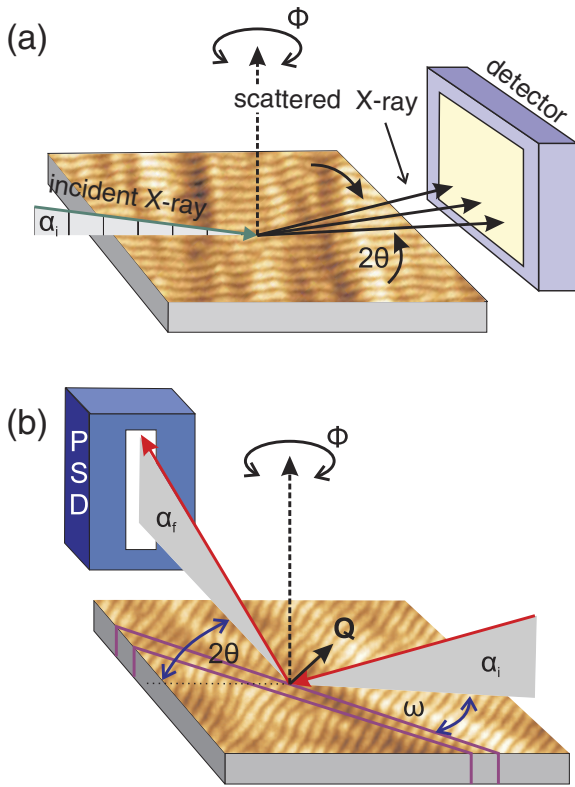
Figure 2. (a) Sketch of the GISAXS geometry. The x-rays illuminate the sample under a shallow angle of incidence and the forward-scattered intensity is detected in the 2D detector plane. (b) Sketch of the GID geometry. Incident and exit angles are small and Bragg's law is fulfilled on lattice planes perpendicular to the surface. A linear sensitive PSD is typically placed perpendicular to the sample surface.

x-ray beam. In the typical hard x-ray regime ($\sim$10 keV), where the x-ray wavelength $\lambda \sim 1$ Å, the magnitude of **q** is of the order of a few nm^{-1} which corresponds to real space distances in the nanoscale range, i.e. 10–100 nm. This makes GISAXS suitable for the investigation of the nanostructure's morphology. Their shape, size, lateral arrangement and ordering are investigated along the direction *perpendicular* to the incoming beam. In the case of isotropic surfaces, one GISAXS measurement at a generic azimuth ϕ is enough to gather information about the morphological parameters of the whole array. In the presence of anisotropy, the GISAXS signal must be recorded at different azimuthal angles ϕ to obtain a 2D intensity map of the surface.

For the GID geometry, the scattering signal is collected at large 2θ angles, i.e. the Bragg angles for a given set of crystallographic planes with the reciprocal lattice vector parallel to the surface. Measuring at large momentum transfer, GID probes small distances (a few Å) and is thus sensitive to the material's atomic structure, including strain and atomic displacements or crystalline defects.

Finally, the components of the scattering vector $\vec{q} = \vec{\kappa}_f - \vec{\kappa}_i$ can be expressed as functions of the three angles $\alpha_{i,f}$ and 2θ in

the following way:

$$q_x^{\text{GISAXS}} = k \cdot (\cos\alpha_f \cdot \cos(2\theta_\parallel) - \cos\alpha_i);$$

$$q_x^{\text{GID}} = k \cdot (\cos\alpha_f \cdot \sin\theta_f + \cos\alpha_i \cdot \sin\theta_i)$$

$$q_y^{\text{GISAXS}} = k \cdot (\cos\alpha_f \cdot \sin(2\theta_\parallel));$$

$$q_y^{\text{GID}} = -k \cdot (\cos\alpha_f \cdot \cos\theta_f - \cos\alpha_i \cdot \cos\theta_i)$$

$$q_z^{\text{GISAXS}} = q_z^{\text{GID}} = k \cdot (\sin\alpha_f + \sin\alpha_i).$$

For the GISAXS geometry the x and y axes are defined as the directions along the beam and perpendicular to it in the plane, respectively. For GID, the y axis is defined to be parallel to the diffracting planes, and θ_i and θ_f are the incidence and exit angles of the x-ray beam with respect to this plane. The z axis is, in all cases, parallel to the surface normal.

2.1. Experimental set-up for GISAXS and GID

Here we will describe the experimental set-up used for GISAXS and GID measurements on beamline ID01 of the ESRF, Grenoble. As a general rule, the scattering geometry is defined as vertical (horizontal) when the vector $\vec{q}$ of the momentum transfer lies in the vertical (horizontal) plane during the measurement. For the special case of GI techniques, this happens when both sample surface and detector lie in the vertical (horizontal) plane. A vertical scattering geometry is generally preferred for measurements with synchrotron radiation due to its small divergence in the vertical plane and its polarization in the horizontal plane. The reduced divergence is reflected in a better angular resolution of the measurement, while the polarization of the synchrotron radiation in the orbit plane (horizontal) introduces a polarization factor in the equation for the scattered intensity, which is responsible for a decrease of the scattering intensity versus scattering angle θ, which varies as $\cos 2\theta$ [25]. However, in the presence of bulky sample environments, geometrical constraints often impose a horizontal scattering geometry, with the sample surface parallel to the horizontal plane. This is the case of *in situ* measurements of surface nanopatterns created by IBS, for which the set-up will be illustrated in more detail in section 2.2. The energy of the incoming x-ray beam, with a typical value in the range 7–12 keV, is determined by an Si(111) double-crystal monochromator. The beam is shaped by a series of focusing elements and collimating slits positioned along the beamline upstream to the sample. The typical spot size at the sample position is $100 \times 100 \ \mu m^2$ and has an intensity of 10^{12-13} ph s^{-1}, for details see the web page of ID01 [26].

Figure 2 illustrates schematically the set-up used for GI experiments. The beam impinges on the sample surface at an incidence angle α_i. A rotation stage with axis perpendicular to the sample surface permits the variation of the azimuth angle ϕ. For GISAXS measurements ϕ is used to align the nanostructures with respect to the incoming beam or to make azimuthal maps. For GID measurements it corresponds to the ω angle of the diffraction geometry, the angle used to align the
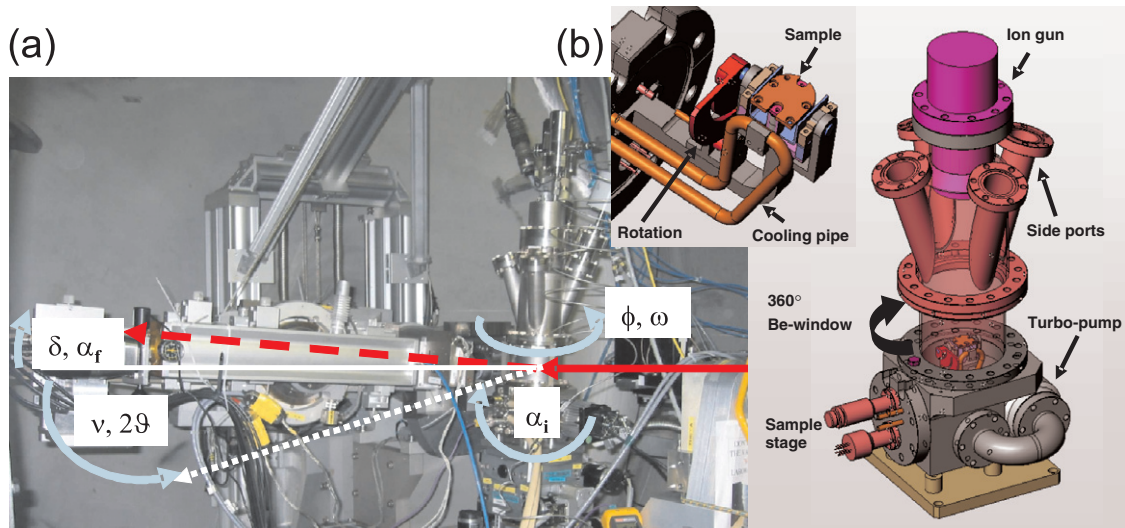
Figure 3. (a) Picture of the *in situ* sputter chamber installed on the diffractometer at the ID01 beamline, ESRF. The angles used for GISAXS/GID measurements are indicated. (b) Schematics of the portable chamber. Reproduced with permission from [27]. Copyright 2008 International Union of Crystallography. See the text for details. Inset: manipulator for IBS experiments. Sample rotation and cooling pipe are indicated.

crystallographic planes to satisfy the diffraction condition for a given value of 2θ.

For the GISAXS measurements (figure 2(a)), the scattering signal is collected using a detector placed in the forward direction, typically on the detector arm of the diffractometer. 1D or 2D position-sensitive detectors are generally chosen. The linear position-sensitive detector (PSD) is usually positioned parallel to the surface (figure 2(b)) at an exit angle α_f. If placed perpendicular to the sample surface, at the level of the sample horizon it collects the scattered signal along the surface normal, i.e. in the direction of α_f, while being moved by the detector arm motor ν to collect the lateral GISAXS signal. A 2D detector does not need to be moved and can collect the $q_\parallel - q_z$ 2D intensity map in a single acquisition.

For GID measurements (figure 2(b)) the scattered signal is collected at large 2θ angles. This requires that the detector arm is rotated in the plane of the sample surface up to the Bragg angle $2\theta_{hkl}$, where (hkl) is the Bragg reflection of interest, expressed in terms of its Miller indices. In this scattering geometry, the sample azimuth is used to align the crystallographic planes to satisfy the diffraction condition, i.e. so that they make an angle $\phi = \theta_{hkl}$ with respect to the impinging x-ray beam in the surface plane. A linear position-sensitive detector is placed perpendicular to the sample surface, at the height of the sample horizon. In this way, the PSD collects the scattering signal transmitted through the surface, along the direction α_f. The angular range covered by the PSD is about $1°–2°$, depending on the distance from the scattering center.

2.2. Sputtering chamber for in situ studies

For *in situ* GISAXS/GID on nanopatterns created by IBS, a compact vacuum chamber is used on ID01 (see figure 3). This chamber, equipped with a 360° Be window around the

sample position and transparent to x-rays in the hard x-ray regime, has been constructed for *in situ* studies of ion-beam-eroded surfaces combined with surface-sensitive x-ray scattering techniques. It is mounted on a heavy-duty sample stage suitable for z-axis scattering geometry at the center of the ID01 diffractometer [27]. The chamber is equipped with a 3 cm diameter Kaufman ion source (supplied by Veeco) that delivers an ion beam with 10° divergence and a current density up to 1 mA cm^{-2} in the low energy range 100–1200 eV. The surface of the sample, at 10 cm from the ion source, can be oriented with respect to the incident ion beam in an angular range between 0° and 90° with an accuracy of $\pm 0.7°$. A cooling system which uses chilled water, coupled with a heating stage, allows for temperature control of the substrate in the range 0–700 °C with ± 1 °C accuracy. A complete description of the chamber can be found in [27].

Figure 3(a) shows a picture of the sputtering chamber mounted on the ID01 diffractometer. The sample surface lies parallel to the horizontal plane; therefore for *in situ* GISAXS/GID measurements the horizontal scattering geometry has to be used. The incident angle α_i is determined by a tilting stage, which rotates the whole chamber in the vertical plane, as indicated in the figure. The exit angle α_f lies in the vertical plane and is defined by the δ motor of the detector arm. The in-plane scattering angle 2θ is defined by the detector movement ν. For GISAXS and GID measurements, the 360° Be window guarantees accessibility to the whole sample surface from any direction, i.e. for any value of the azimuth angle ϕ and any value of the scattering angle 2θ.

3. Data evaluation

The interpretation of GISAXS and GID spectra collected on nanopatterned surfaces relies on the use of an appropriate fitting model. In this section we describe the characteristics

of the diffuse intensity produced by self-organized surface nanostructures in the reciprocal space, which are the basis for the GISAXS (and GID) signal. We will illustrate how to interpret this intensity distribution, introduce the tools to model it and the different information we can extract. In principle, the models and the data analysis for interpreting GISAXS and GID data are the same, keeping in mind, however, that GISAXS is only sensitive to the morphological parameters (i.e. length scales of a few nm), while GID also includes information about atomic distances (crystal structure, presence of strain and crystalline correlations). In particular, this means that any asymmetry of the intensity distribution in the reciprocal space around $Q = 0$ (i.e. the GISAXS signal) can only be determined by a shape asymmetry in real space, while the presence of asymmetry in a GID spectra (i.e. around Bragg reflections (hkl)) has to be carefully analyzed, as it could depend on both shape asymmetry and strain in the crystal lattice.

3.1. Diffuse scattering from nanostructures in the kinematical approach

X-rays are electromagnetic waves described by a wavevector of amplitude $\kappa = 2\pi/\lambda$, where λ is the x-ray wavelength, related to the x-ray energy E_X by the relation $\lambda[\text{Å}] = \hbar\omega/c^2 = 12.398\,74/E_X[\text{keV}]$. The interaction of x-rays with matter is mediated by the electrons present in the material. In the case of elastic scattering, which is the case we consider here, the energy is conserved and only the direction of the exit wave κ_f is changed by the scattering event. The produced momentum transfer $\vec{q} = \vec{\kappa}_f - \vec{\kappa}_i$ has an amplitude that depends on the scattering angle θ, $q = 4\pi \sin\theta/\lambda$, probing a real space distance $d = 2\pi/q$. Therefore, x-ray scattering probes electron densities and electron distributions at different length scales, depending on the value of the total momentum transfer, i.e. of the scattering angle θ. In the kinematical approach, the scattering amplitude at a point q of the reciprocal space can be expressed as

$$A(q) = A_0 r_0 P \frac{e^{i\kappa R}}{R} \int \rho(r) e^{iq \cdot r} \, dV \qquad (5)$$

where A_0 is the amplitude of the incoming wave, $\rho(r)$ the electron density of the material at the point r, P is the polarization factor and R is the distance where the signal is collected, e.g. the distance between sample and detector, and the integral is performed over the illuminated volume. From equation (5), the measured intensity is

$$I(q) = \frac{|A(q)|^2}{|A_0|^2} R^2 = r_0^2 P^2 \left| \int \rho(r) e^{iq \cdot r} \, dV \right|^2. \qquad (6)$$

For the special case of nanostructures, the scattering intensity comes from the interaction of x-rays with the electron density distribution within each nano-object and with the ensemble of objects illuminated (coherently) by the same x-ray beam, therefore from the sum of x-ray waves scattered by adjacent objects. In this case, positional correlation of the structures can lead to interference between the scattered waves from the individual objects. To take into account this positional

correlation, the amplitudes A_m^{diffuse} from objects at positions $\mathbf{R}_m$ can be summed up coherently. The total scattering amplitude is then given by

$$A_{\text{total}}^{\text{diffuse}}(\mathbf{q}) = \sum_m A_m^{\text{diffuse}}(\mathbf{q}) e^{i\mathbf{q}\cdot\mathbf{R}_m}.$$

This approximation is valid as long as the distance between the objects is sufficiently larger than their size. However, it can also be applied in the case of close packed structures, if one assumes that the scattering objects are sufficiently similar, i.e. they have the same shape and orientation and a narrow size distribution. In this case, the amplitudes A_m^{diffuse} are identical and the expression for the diffuse amplitude becomes

$$A_{\text{total}}^{\text{diffuse}}(\mathbf{q}) = A^{\text{diffuse}}(\mathbf{q}) \sum_m e^{i\mathbf{q}\cdot\mathbf{R}_m}$$

and the intensity at a point q of the reciprocal space becomes

$$I(q)_{\text{total}} = |A^{\text{diffuse}}(\mathbf{q})|^2 \cdot S(q) \qquad (7)$$

that is, the product of the square of the amplitude generated by a single object times the interference among all the objects illuminated, $S(q)$:

$$S(q) = \left| \sum_m e^{i\mathbf{q}\cdot\mathbf{R}_m} \right|^2 = \sum_{m,n} e^{i\mathbf{q}\cdot(\mathbf{R}_m - \mathbf{R}_n)}.$$

It can be shown [28] that the interference function in reciprocal space can be expressed as the Fourier transform of the positional auto-correlation function of the nano-objects $C(r)$ in real space:

$$S(q) \sim \int C(r) e^{iq\cdot r} \, dV \qquad C(r) = \int \rho(r') \rho(r + r') \, dV'. \qquad (8)$$

On the other hand, the diffuse scattering produced by a single object $A^{\text{diffuse}}(q)$ can be calculated from equation (5) using the following expression for the electron density of an object m at a position R_m:

$$\rho(r) = \rho_0 Sh(r - R_m)$$

where ρ_0 is the average electron density of the object and $Sh(r - R_m)$ is its shape function, which assumes a value of 1 in its interior and 0 outside. The scattered intensity (6) from a single nano-object becomes

$$I(q) = r_0^2 P^2 \rho_0^2 |F(q)|^2$$

where $F(q)$ is the nano-object form factor, defined as the Fourier transform of the object shape function $Sh(r)$, while total intensity scattered by an ensemble of nano-objects (7) becomes

$$I(q)_{\text{total}} = r_0^2 P^2 \rho_0^2 |F(q)|^2 S(q) \qquad (9)$$

where the hypothesis of structures with the same shape and a small size distribution is always valid. If the particles have a certain shape and size distribution, as is often the case for self-organized structures created by IBS, the function $|F(q)|^2$ can be replaced by the statistical average $\langle |F(q)|^2 \rangle$. As an example, $\langle |F(q)|^2 \rangle$ for cylinders of radius R and different width of the R distribution is given in figure 6 (top).
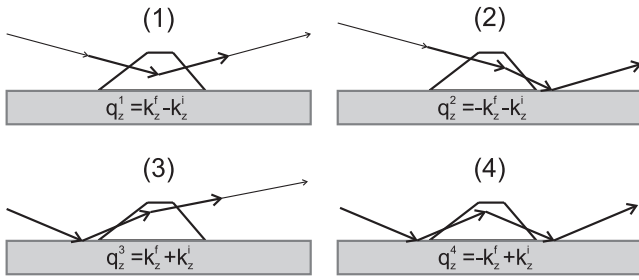
Figure 4. The four scattering events considered in the distorted wave Born approximation from freestanding islands on a surface together with their vertical momentum transfers according to equation (10).

3.2. Distorted wave Born approximation

In the previous section, only kinematical scattering has been considered; multiple scattering events have been neglected. This approach is very powerful for strongly disturbed systems, but is often not sufficient for the treatment of rather perfect semiconductor systems, which is the case of the structures studied in this paper. Furthermore, in the case of GI scattering techniques the specular beam is also scattered diffusely, leading to enhanced intensity in its vicinity. This specular beam is missing in the kinematical theory. On the other hand, dynamical theory is also not applicable because in most cases there is no exact solution for the scattering equations due to the statistical character of the nanostructure arrangement; therefore, the so-called distorted wave Born approximation (DWBA) is used. The DWBA is well known from quantum mechanics as a perturbation expansion of the scattering equation. For the description of GISAXS intensities, four distinct scattering events have to be considered, as illustrated in figure 4. Rauscher *et al* [29] showed that, for freestanding nanostructures, the scattering cross section can be written as

$$\frac{\mathrm{d}\sigma}{\mathrm{d}\Omega}(\mathbf{q}) = r_0^2 \rho_0^2 |F(\mathbf{q}_\parallel, q_z^1) + r_\mathrm{f} F(\mathbf{q}_\parallel, q_z^2)$$
$$+ r_\mathrm{i} F(\mathbf{q}_\parallel, q_z^3) + r_\mathrm{i} r_\mathrm{f} F(\mathbf{q}_\parallel, q_z^4)|^2 S(\mathbf{q}) \qquad (10)$$

where $q_z^1 = k_z^\mathrm{f} - k_z^\mathrm{i}$, $q_z^2 = -k_z^\mathrm{f} - k_z^\mathrm{i}$, $q_z^3 = k_z^\mathrm{f} + k_z^\mathrm{i}$ and $q_z^4 = -k_z^\mathrm{f} + k_z^\mathrm{i}$.

Thus, the total scattered intensity is calculated as a coherent sum of the partial scattering amplitudes for the single events that may interfere with each other.

Equation (10) holds for each reciprocal lattice point; therefore it can be used to understand the diffuse intensity around the origin of the reciprocal space (GISAXS region) as well as around any Bragg peaks, measured in GID geometry. As an example, a schematic view of the (in-plane) intensity distribution in reciprocal space generated by a one-dimensional surface grating is given in figure 5(a). The main difference between the origin of reciprocal space (the (000) reciprocal lattice point) and a generic (*hkl*) point is that, in the case of a Bragg peak, the diffuse signal, like the Bragg peak itself, arises from the crystalline part of the sample, whereas it is independent of crystal structure at the origin.
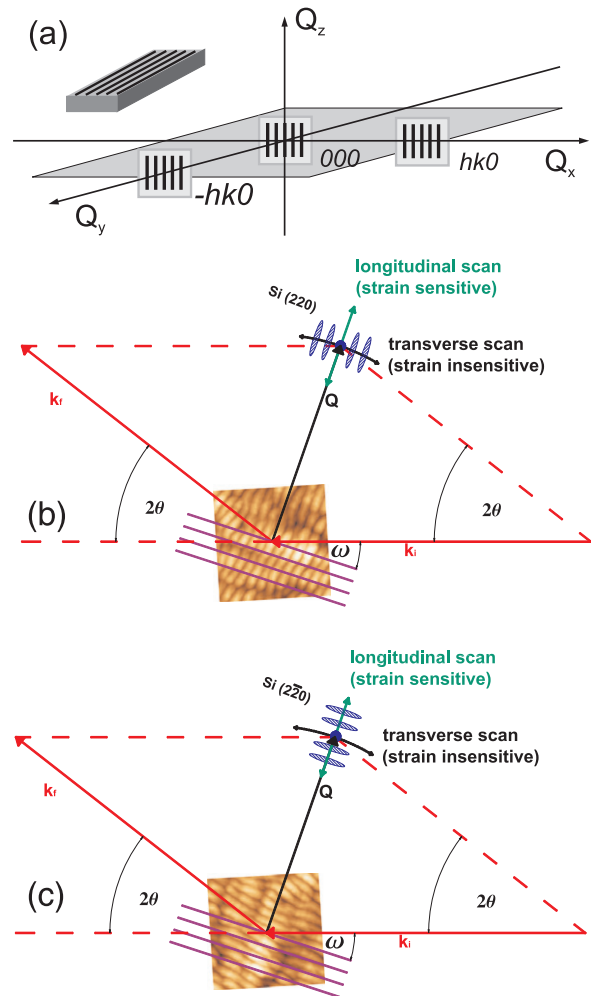

Figure 5. (a) Sketch of the (in-plane) reciprocal space created by a periodically patterned crystal. The Bragg peaks accessible in GID geometry are surrounded by satellite peaks imposed by the periodic structure. ((b), (c)) Transverse and longitudinal scans at two symmetry-equivalent GID reflections. For a rippled substrate, satellite peaks show up only in one of the two scan directions.

3.3. Scans in reciprocal space

When performing scans in GID geometry, one usually refers to two different kind of scans. The first one, the so-called transverse (or angular) scan, is realized by rotating the sample around its surface normal (ϕ, ω), i.e. perpendicular to the diffraction plane, and keeping the scattering angle 2θ fixed. This keeps the length of the scattering vector **q** fixed and corresponds mainly to a scan in q_y (figures 5(b) and (c)). This scan is not sensitive to information from strained material inside the crystal, because compressed or expanded material gives rise to intensity at other scattering vector lengths. In the second type of scan, the longitudinal (or radial) scan, the sample is again rotated around its surface normal (ϕ, ω) but, at the same time, the angle 2θ is changed twice as much. This means that the length of the scattering vector changes while the direction of **q** in reciprocal space is fixed. Because q is changed, this scan is sensitive to the distribution of the lattice parameter d inside the crystal, according to the implicit Bragg
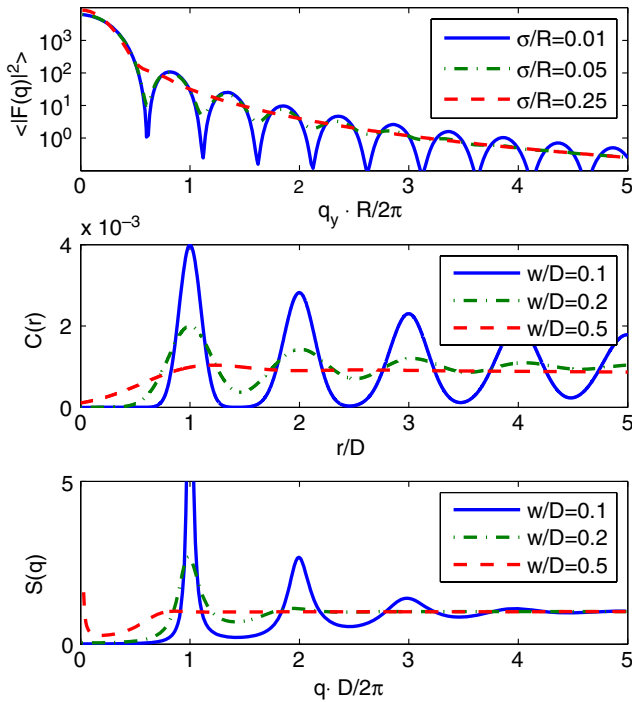
Figure 6. (Top) Form factor of a cylinder for different widths of the Gaussian radius distribution. (Middle) Particle autocorrelation function $C(r)$ for various widths of the next-neighbor distribution. (Bottom) Interference function $S(q)$ corresponding to the correlation function $C(r)$.

equation $q = (4\pi/\lambda)\sin\theta = 2\pi/d$. Figures 5(b) and (c) illustrate schematically the scan directions around an in-plane Bragg peak that is surrounded by satellite peaks caused by a periodic ripple structure. If the ripple pattern is aligned along the [110] direction of the substrate, the satellites can show up either in the longitudinal or transverse scan, depending on the sample orientation.

3.4. Modeling GISAXS/GID data

From equation (9), we see that the diffuse intensity around an (*hkl*) point in reciprocal space depends on the shape of the nanostructures, via the form factor $F(q)$, and the positional correlation $C(r)$, via the interference term between waves scattered by different nanostructures $S(q)$ (cf equation (8)). Therefore, to model the diffuse intensity in the reciprocal space originating from an assembly of nanostructures, one needs to define their shape and the type of positional correlation in real space. The shape function is determined by the real space geometry of the object, while the spatial correlation function has to be modeled in an appropriate way. We present here three main types of possible ordering which might occur for self-organized nanoparticles on a surface. The first, a very local, liquid-like ordering, presents only a nearest-neighbors correlation. A second type of short-range order extends to a certain number of particles within a region that can be considered as locally ordered, or uniform. A third type of order, the long-range type, is the regular lattice, where the particles lie at the corners of a regular mesoscopic structure. In

this case one can talk about lattice symmetry, size of ordered domains, that might range from a few times the 'lattice unit' to the whole investigated surface.

One of the most appropriate models for self-organized nanostructures, which rarely have a perfect lateral arrangement that can be approximated to a crystal-like structure, is the paracrystal model, where the lateral order is gradually destroyed with distance. This model bridges the two extreme cases of ordering: the regular lattice and the fully disordered structures. In the case of a local order extending to one nearest neighbor, the SRO merges into the liquid-like model. The details of this model can be found in the manual of *IsGISAXS* [30]. Here we restrict ourselves to the description of the main parameters. The probability of finding a particle at a distance *x* from a given particle chosen as the origin is given by a Gaussian distribution, with *D* as the average value and *w* as the dispersion. As a consequence, the probability of finding the second-next particle at a distance *y* is given by the self-convolution of this probability distribution, which is again a Gaussian, but with a larger width. After several of these convolutions, the position of the *n*th particle becomes completely unpredictable $w \sim D$. Finally, the interference function in reciprocal space is obtained by calculating the Fourier transform of the probability distribution. The smaller *w* is, the larger the number of particles lying in an ordered region of the surface. The larger *w*, the more disordered the pattern becomes. *w* is therefore used to estimate the size of the 'ordered' or uniform region of the pattern ξ. For the SRO model, this is given by the relation $\xi = \langle D \rangle^3 / 2w^2$ [28]. As an example, figure 6 shows the one-dimensional particle probability distribution, i.e. the auto-correlation function, for various widths of a Gaussian next-neighbor distribution according to the paracrystal model. The lower part of figure 6 shows the corresponding interference function in reciprocal space.

One has to point out that the correlation length ξ has to be understood as a measure for the uniformity of the pattern rather than the size of an ordered domain. Contrary to this, the correlation length or domain size is obtained in most AFM studies by taking the inverse of the FWHM of the first-order peak in the power spectral density, without any model for shape or correlation of particles. However, this describes the domain size in a long-range order scenario. Here, the order is assumed to be almost perfect ($w \to 0$) in domains of size ξ. The broadening of the correlation peaks is then due to the finite-size broadening imposed by truncation of the almost perfect order after length ξ. Although this is a good approach for highly ordered systems, it can be misleading when applied to rather nonuniform systems like most dot patterns created by IBS. Besides the different statistical sampling of both techniques, this model-dependent discrepancy always has to be taken into account when comparing correlation lengths obtained by a simulation of GISAXS data and most AFM analysis.

A second important point that needs special attention when analyzing GISAXS data is the amount of information one can retrieve from it. In many experiments, only line sections through reciprocal space are analyzed for the sake of simplicity. As long as the decomposition of correlation and

shape, as described above, is valid, this approach is capable of obtaining information about lateral correlation, but the actual shape of the particles can, in most cases, not be retrieved uniquely. For instance, if one approximates dots produced by IBS as cones, at least the parameters radius, height and facet angle together with their distributions have to be considered when calculating the form factor. However, a measurement at fixed q_z is not suited to retrieve information unambiguously about the height of the particle. Therefore, fitting of the data by a computer simulation can often be achieved equally well by different choices of the above parameters. The situation is different when two- or even three-dimensional datasets are analyzed, as it becomes, to some extent, possible to retrieve detailed information about the (average) shape of the particles. An example of this is shown in section 5. The strength of the GISAXS analysis compared to AFM is therefore the separation of form factor- and correlation-induced diffuse scattering, which allows us to obtain information about the particles' correlation with statistical sampling of an area up to several hundreds of μm^2, compared to only a few μm^2 with AFM.

4. Results: low energy IBS

This section is dedicated to the results of *in situ* and *ex situ* x-ray studies of nanopatterns created on semiconductors by IBS in the low energy regime, i.e. 100–2000 eV. The characteristics of the patterns created in this way are, on the one hand, the small size and periodicity of the nanostructures and, on the other, the limited 'damage' done to the crystal structure by the erosion process. Concerning the nanostructure's size, typical values are in the range of 10–50 nm, depending on the material and the ion energy; their height is of the order of 1–10 nm. The 'damage' to the crystal structure can be expressed in terms of the creation of a thin amorphous layer at the surface, of the order of 1–5 nm. In addition, lattice strain and deformations may develop and can be characterized using GID.

4.1. Ex situ studies

The systems we will discuss in the following sections consist in dot and ripple morphologies obtained on Si and Ge surfaces, using Ar or Xe ions. The first study we refer to is the time evolution of the morphological parameters of nanodot patterns created on Si(001) and Si(111) surfaces by Ar^+ ions at normal incidence [31]. We will also discuss the dependence of the final morphology on the substrate temperature for nanodots created on Si(001) surfaces at fixed ion dose [32]. Ripple morphology on Ge(001) substrates created under off-normal incidence of Xe^+ ions is the second system studied *ex situ*. In this case the attention is focussed on the early-time behavior of the ripple formation. A combination of GISAXS and AFM revealed that the ripples originate from the coalescence of isolated dots formed in the first moments of ion erosion [33]. The third case reported here is the study of highly ordered ripples on Ge and Si surfaces obtained after off-normal Xe- and Ar ion erosion, respectively [34].

4.1.1. Time evolution of Si nanodots under normal Ar^+ incidence.
This work was aimed at comparing the time evolution and the final morphology of nanodot patterns induced by Ar^+ erosion on Si(001) and Si(111) surfaces [31]. As the nanopatterning of semiconductor surfaces is thought to start from a process of amorphization of the surface, it is expected that the crystal structure of the surface does not play a role in the final pattern morphology. In agreement with this prediction, the pattern dynamics are found to be qualitatively independent of the surface orientation.

The Si surfaces were eroded by Ar^+ ions at 1.2 keV under normal incidence on a set of samples, using increasing ion dose as described in [31]. GID measurements were performed *ex situ* on all the samples, using an x-ray wavelength of 1.55 Å and an incidence angle of 0.2°, slightly below the critical angle for total external reflection (0.22°), to increase the surface sensitivity of the measurement. The exit angle resolved intensity was integrated along a position-sensitive detector placed perpendicular to the sample surface. Therefore line scans of the type $I(q_{x,y})$ were obtained, rather than reciprocal space maps $I(q_{x,y}, q_z)$. Measurements in reciprocal space were taken around the in-plane (220) and (2$\bar{2}$0) Bragg reflections for Si(001) and Si(111), respectively.

The evolution of the correlation distance λ is analyzed from GID data. Figure 7(b) shows the GID angular scans for both surfaces at increasing ion dose. The presence of correlation peaks around the measured Bragg positions reveals both the pattern formation and the crystalline character of the nanodot structures [35]. The distance of such peaks from the Bragg position decreases as the ion dose increases, indicating a coarsening of the nanostructures. Additionally, the correlation peaks become more intense and sharper with ion dose, indicating an enhancement of the lateral ordering. The absence of an asymmetry in the GID radial scans at the Bragg position (not shown here) excludes the presence of strain in the crystalline core of the dots. The quantification of λ and ξ by GID is done through a spectral fitting as described in section 3. GID data analysis indicates that the evolution of the pattern wavelength saturates earlier for Si(111) surfaces. Both crystal orientations show, however, a clear coarsening of λ with ion dose. Moreover, the data show ordering enhancement with ion dose, as qualitatively reported previously for GaSb, InP and Si patterns by means of AFM [36, 37, 13]. The Si(111) surface is found to reach a stationary state at lower dose. This result is attributed to the larger sputtering rate measured for this orientation, which is observed to be ~10% higher for Si(111) than for Si(001). It is important to note that the surface with lower sputtering rate shows a slower dynamics but reaches larger ordered domains in the saturation limit. The dependence of the pattern formation on the sputtering rate and the temporal evolution of the pattern features reported here have also been observed by *in situ* synchrotron studies on GaSb surfaces [18] (section 4.2). Finally it should be mentioned that the same samples have also been investigated by AFM. The results are comparable with those from the GID study, but show intrinsically a worse statistical sampling.

Some x-ray studies on the formation of nanostructures on Si, and especially on the role of metal seeding, have been
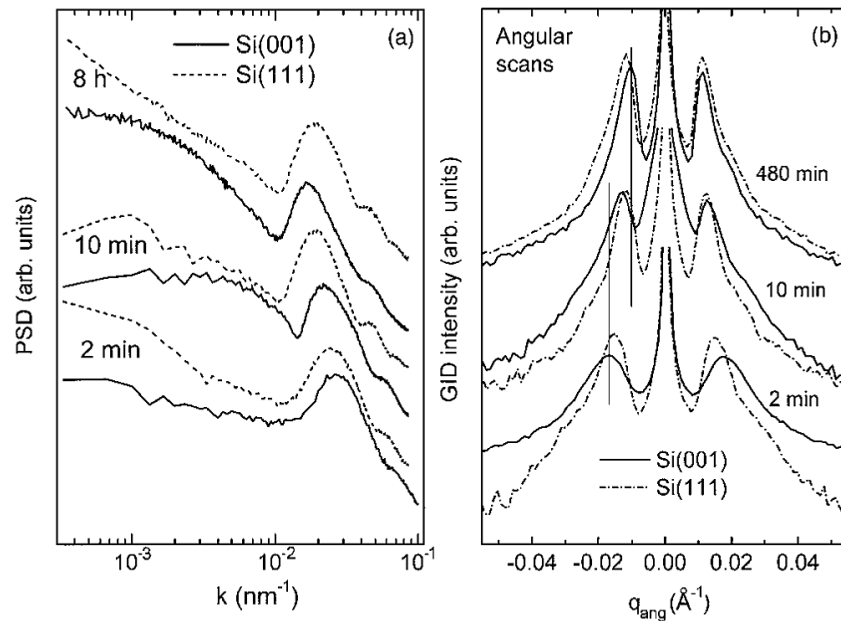
Figure 7. (a) PSD from AFM images and (b) GID angular scans of Si(001) (solid lines) and Si(111) (dotted lines) sputtered for 2, 10 and 480 min. The spectra have been shifted vertically for clarity and the GID intensity is shown in logarithmic scale. The vertical lines are guides for the eyes to show the peak shift [31]. Reproduced with permission from [31]. Copyright 2006, American Institute of Physics.

performed by other groups [38, 39]. The main observation was that Si surfaces without any metal incorporation develop only power-law roughness during 1 keV Ar$^+$ bombardment at normal incidence but no nanostructure formation. Instead, the incorporation of Mo from the surroundings, in this case clips to fix the sample, leads to the development of highly correlated nanodots. These show coarsening and saturation with ion fluence, as investigated by *in situ* GISAXS measurements. One possible explanation for the Mo seeding effect for the nanodots is the sputtering yield variation on the surface under ion bombardment that is induced by an inhomogeneous surface chemistry. Indeed, for 1 keV ion bombardment, Mo has a higher sputter yield than Si. The formation of molybdenum silicides on the surface may create zones with a reduced sputter yield. This preferential sputtering may also explain why the dot formation process is much more efficient on surfaces such as GaSb and InP, as compared to pure Si or Ge. Another possible explanation for this effect could be a seed-atom-induced surface stress which can be investigated by GID. These results give some clues in understanding previous results obtained where no pattern formation was obtained during sputtering a Si(100) surface under normal incidence [40]. The role of metal incorporation in the pattern formation has been addressed again in a recent work [41] in the context of the selective production of nanodot and nanohole patterns versus the density of the ion current. It was found that the metal content (Fe or Mo) in the nanohole patterns is about twice as high as compared to the nanodot patterns. It can then be inferred that the surface composition as well as the dependence of the erosion rate on the ion flux and surface topography is of major importance for a complete theoretical description of the surface evolution under ion bombardment.

Recently Ozaydin *et al* performed *in situ* GISAXS on Si(001) without metal seeding and revealed that the surface remains smooth up to 400 °C during 1 keV Ar$^+$ ion bombardment under normal incidence [42]. In that case, no pattern was obtained on the surface. In addition the near-surface area was amorphized by the ion bombardment as observed with *in situ* RHEED. Kinetic roughening was shown to develop for temperatures between 400 and 500 °C. Above 500 °C the near-surface region was shown to remain crystalline under irradiation and the roughness correlation wavelength showed a power-law behavior. This roughness growth behavior at elevated temperature is similar to a metal's behavior under ion bombardment and suggests the presence of a surface diffusion-mediated mechanism. On the other hand, the low temperature results might be understood by the lack of metal incorporation in the surface.

In the light of these results, some of the past work should possibly be re-analyzed to estimate the metal contamination (intentional or not) of the patterned surfaces. Some of the Si samples discussed in sections 4.1.1 and 4.1.2 have been re-investigated with chemically sensitive methods to this aim [41]. In these samples Fe and W traces have been detected, probably coming from the ion source filament or the sample holder. However, the detected quantities are appreciably lower than those reported in [39]. These results open the question whether the presence of materials with different sputter yield on the surface is essential in the nanopatterning process, or to what extent the presence of impurities influences the pattern formation under IBS.

4.1.2. Temperature dependence of Si nanodot formation at fixed Ar$^+$ ion dose. The role of the substrate temperature T during ion erosion can be significant in the nanostructuring process by governing surface diffusion processes and has been addressed in several studies. In the case of GaSb surfaces [43],
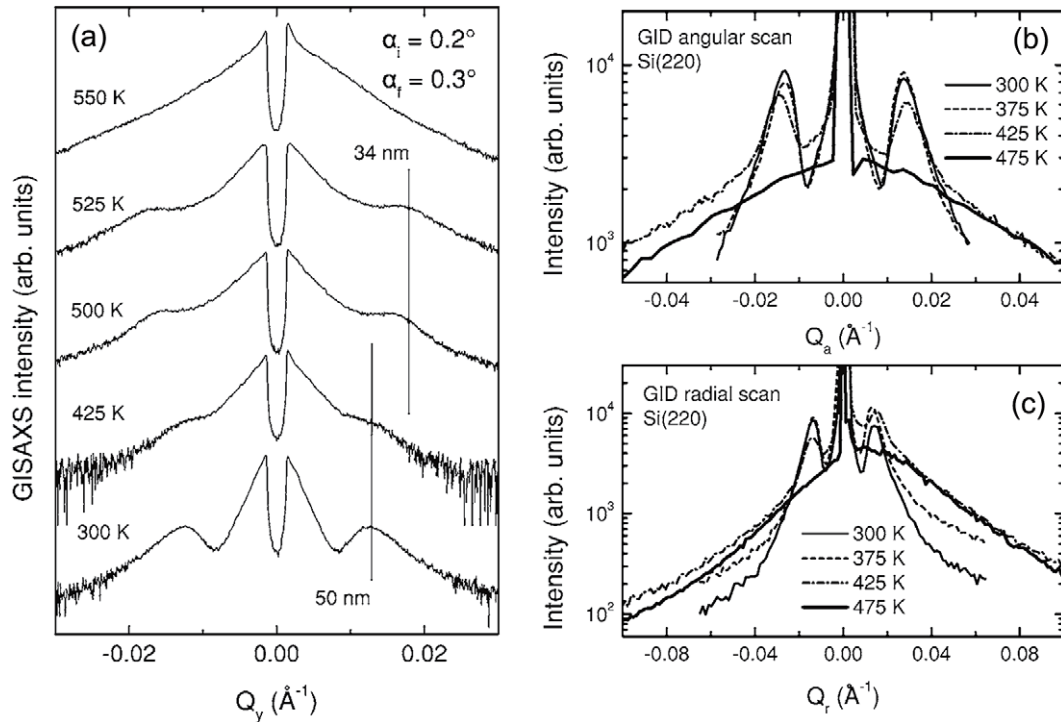
Figure 8. (a) GISAXS scans obtained from Si(001) substrates sputtered with 1 keV Ar$^+$ ions for 10 min at 300, 425, 500, 525 and 550 K. (b) GID measurements around the (220) in-plane Bragg peak in angular and (c) radial directions from Si(001) substrates bombarded under normal incidence by 1 keV Ar$^+$ ions for 10 min at 300 K (thin solid line), 375 K (dashed line), 425 K (dashed–dotted line) and 475 K (thick solid line) [32]. Reproduced with permission from [32]. Copyright 2006 The American Physical Society.

no appreciable effects in the pattern formation were observed in the 213–333 K range, suggesting the dominance of ion-induced diffusion processes [44]. On the contrary, the formation of InP nanodots within the 268–335 K range has shown an increase of both interdot distance and dot height with T and an interesting change in the pattern ordering from hexagonal-like to square-like at 335 K [45]. However, to date, no theoretical explanation has been given for these observations. We discuss here an x-ray study of the influence of substrate temperature on the production of nanodot patterns on Si(001) surfaces by IBS, in a wide temperature range, 300–625 K. The added value of the x-ray scattering is the evaluation of the relative contribution of the crystalline and amorphous parts to the dots.

Si(001) substrates were sputtered with 1 keV Ar$^+$ ions at normal incidence in the temperature range 300–625 K. The total erosion time was set to 10 min such that the surface morphology has reached a stationary state [19]. GID measurements were performed as described in section 2.1. The diffuse intensity around the in-plane Si(220) Bragg reflection was recorded with a linear position-sensitive detector mounted perpendicular to the sample surface. In order to isolate the morphological contribution to the diffuse scattering, GISAXS scans were recorded in the forward direction. The angle α_i was set at 0.2° to enhance the signal and the GISAXS spectra were measured at $\alpha_f = 0.3°$.

In figure 8(a) the correlation maxima in the GISAXS scans are observed in all the Si(001) surfaces processed at temperatures below 525 K. The corresponding interdot

distance is $\lambda = 50$ nm for temperatures up to 425 K and decreases continuously down to ~30 nm up to 525 K. A decrease of the peak intensity for $T > 525$ K indicates the progressive deterioration of ordering within the pattern. Figure 8(b) shows the evolution of the GID angular scans around the Si(220) Bragg peak as a function of T. The behavior of GID follows closely the GISAXS results up to $T = 425$ K. For temperatures above 475 K, however, the correlation peaks in GID scans disappear completely, while they are still present in the GISAXS scans. However, the persistence of a broad tail in the GID scan coming from the contribution of the form factor of crystalline dots is an indication that the crystalline cores of the dots are partially amorphized, thus leaving some randomly distributed, uncorrelated crystalline dots behind, as also confirmed by HRTEM observations [32]. Figure 8(c) shows the GID radial scans corresponding to the same samples as in figure 8(b). In this case, information about strain in the crystalline lattice of the dots can also be extracted. The asymmetry in the spectral shape indicates a change from tensile to compressive stress ($\Delta a/a = -0.45\%$) in the crystalline core of the dots between the low and high temperature regime.

The GID spectra in figure 8 for T above 375 K show a change in the slope at higher $|Q|$ values, indicating a change in the form factor of the nanostructures. In particular, the broader shape of the scan indicates a decrease in the lateral dimension of the crystalline core. This trend, together with the absence of correlation peaks, can be associated with the decrease of the dot height. In order to estimate the extent of this change, the

GID spectra have been fitted assuming a simplified cylindrical dot shape to calculate the form factor. The fitting procedure also takes the size distribution of the dots into account. Under the above assumptions, the crystalline dot mean size is about four times smaller at 475 K than at 300 K. Finally, the fact that the correlation peak in GID disappears at lower temperatures (475 K) than in GISAXS (550 K) indicates the increase in the relative contribution of the topmost amorphous layer to the dot morphology for $T = 400$ K. Although the nanodots are still present at 475 K, the lack of correlation in GID at 475 K indicates a reduced crystalline volume that contributes to the GID scattering signal. To summarize: in the low-T range (400 K), the pattern is not significantly affected by T and the interdot distance remains constant at 50 nm. Within the 425–500 K range, both the characteristic length and average height of the dot pattern decrease with T. This behavior continues up to 525 K, where an abrupt change of the surface morphology takes place. Still, a sort of dot morphology is present with dot height slightly larger than the crystalline dot core, as supported by the presence of a form factor in the GID spectra and no correlation peaks above 475 K. When T is further increased by only 25 K, the dot pattern completely vanishes. In this regime, the surface morphology becomes flat and featureless.

4.1.3. Early-time behavior of ripple formation on Ge at off-normal Xe$^+$ ion beam erosion. We present a study of the early stage of ripple formation on Ge(001) surfaces irradiated by a 1 keV Xe$^+$ ion beam at room temperature and near-normal incidence. We observe that the isotropic dot pattern formed during the first minutes of sputtering evolves into an anisotropic ripple pattern for longer sputtering time. The peculiarity of these results is that this transformation occurs at room temperature, as a function of the ion fluence only, while other parameters such as angle of incidence of the ion beam, substrate position, temperature and ion beam flux were kept constant. These results provide a new basis for further steps in the theoretical description of the morphology evolution during ion beam sputtering.

For this study, Ge(001) substrates were irradiated with a Xe$^+$ ion beam at 1 keV at a fixed angle of incidence $\theta_{ion} = 10° \pm 1°$ as described in [33]. Different samples were produced by varying the erosion time between 1200 and 7200 s, corresponding to a range of fluences between 4.1×10^{17} and 2.4×10^{18} cm^{-2}. GISAXS profiles were measured at an x-ray energy of 9 keV. The measurements were performed at an incident angle $\alpha_i = 0.3°$, slightly larger than the Ge critical angle for total external reflection ($\alpha_c = 0.275°$) using a beam of 200×100 μm^2 (horizontal and vertical size). Data were acquired by a linear detector placed parallel to the sample surface, with a beam stop at the position of the plane of incidence to prevent detector saturation. Due to the anisotropy of the process. i.e. the off-normal erosion conditions, we decided to investigate the patterning process along the directions parallel and perpendicular to the ion beam direction. To this end GISAXS measurements were performed along the two anisotropy directions for four samples eroded in the same conditions, but with different values of fluence

(increasing erosion times). AFM investigations were used to complement the x-ray scattering data.

Figure 9(a) shows GISAXS profiles performed along the two anisotropy directions of the samples, compared to power spectral density (PSD) curves calculated from AFM images. Due to the anisotropy of the surfaces, we calculated the PSD from linear averaging of the $|FFT|^2$ along the two anisotropy directions, i.e. parallel and perpendicular to the ion beam, rather than from the usual angular averaging. At low fluence (continuous curve in the top panels of figure 9, $t = 1200$ s) in the direction of the impinging ions, we observe, in both PSD and GISAXS curves, correlation maxima which reveal the presence of nanostructures with average distance $\lambda \sim 42$ nm. The GISAXS signal measured in the direction perpendicular to the ion beam (solid line) does not show correlation maxima. Instead, it is dominated by the form factor of the surface structures and can be fitted using a model of uncorrelated cone-shaped structures with average lateral size of 10 nm with a very broad size dispersion $\delta R \sim 12$ nm. This indicates that, at low fluence, dots form on the Ge surface, with a short-range order along the direction of the impinging ions and no spatial correlation in the direction perpendicular to it. With increasing fluence (filled and open dots in figure 9 for $t = 2400$ and 7200 s, respectively), we observe a progressive sharpening and the appearance of higher-order correlation peaks in both GISAXS and PSD profiles in the direction of the ion beam. In the perpendicular direction only very broad ordering peaks are observed, which do not evolve with time. This indicates, on the one hand, the increase of the nanostructure's order along the direction of the impinging ions, and on the other, the persistence of structures with a weaker lateral order in the direction perpendicular to it. These measurements confirm that a morphological anisotropy develops with time during the IBS process, giving rise to a surface characterized by ordered ripples transversal to the ion beam direction, interrupted by weakly correlated dots.

The GISAXS curves discussed above have been analyzed with the software *IsGISAXS* [30] using a model of short-range order, where lateral size D, mean distance λ and lateral correlation length ξ of the nanostructures have been used as fitting parameters. The results of this fitting procedure are summarized in figure 9(c). While the average lateral periodicity is similar for dots and ripples, with $\lambda \sim 43$ nm, the lateral order is very different in the two directions, being very weak for the dots and more pronounced for the ripples. The lateral correlation for the dot structures extends over a distance of $\xi \sim 105$ nm, which corresponds to about two nearest neighbors. For the ripples it increases dramatically with fluence, rising from $\xi \sim 400$ to 1500 nm, i.e. from ~10 to ~37 nearest neighbors. In the framework of the SRO model, we interpret the correlation length as a measure of uniformity of the ripple pattern, rather than a measure of the size of ordered domains. Even though the alignment is not perfect or periodic, the ripples make an uniform ordered pattern where the mutual distance λ is preserved over a large distance. The observation of increased order for ripple structures as a function of fluence is in agreement with theoretical predictions [46].

The results presented in our work represent a rare case of transient morphology of nanopatterns observed during ion
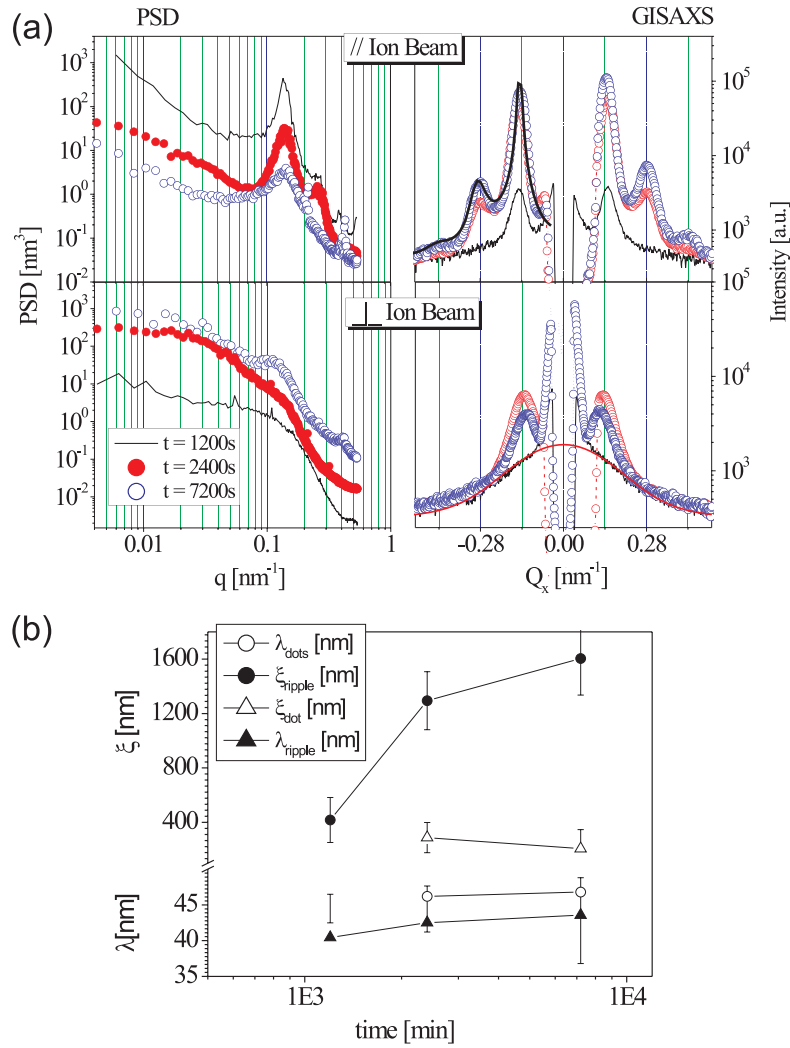
Figure 9. (a) Comparison between PSD obtained by linear averaging (see text) parallel and perpendicular to the ion beam and corresponding GISAXS profiles for different erosion times. Some fits of GISAXS data are exemplary shown by the solid lines in the right panels. (b) Time dependence of average distance λ and size of ordered domains ξ parallel and perpendicular to the ion beam direction. The order of the nanostructures along the ion beam (ripples) increases with fluence, while in the perpendicular direction it stays weak and constant [33]. Adapted from [33]. Copyright 2008 IOP Publishing Ltd.

beam sputtering [15], which is not fully accounted for by current theories. In our interpretation, the ripples created on Ge by off-normal IBS result from a coalescence of the dots that are created in the early stage of erosion. A validation of this model can be found in the peculiar shape of the final ripples, which preserve the morphology of the dots in their undulated profile. One attempt to investigate theoretically the short-time behavior of sputtered surfaces for ripple formation is presented in [47]. The authors calculate a phase diagram for transient morphologies in ripple formations upon variation of the longitudinal and lateral straggle. In a small region of the phase diagram, a morphologic transition from a 2D to 1D pattern is predicted with increasing ion fluence, which is qualitatively similar to our data. However, in this case the pattern evolves from holes to ripples.

4.1.4. Highly ordered patterns obtained on Si and Ge by low energy noble gas sputtering. In this section results of *ex situ* GISAXS and GID studies performed on nanostructured Ge

and Si surfaces will be presented. A representative example of such a patterned surface is given in figure 10. The AFM image shows well-aligned ripple patterns on Si(001) forming normal to the ion beam direction (arrow in figure 10). The FFT image reflects the very good alignment of ripples resulting in a multiple number of peaks.

Ripples on Ge. A representative example of GISAXS and GID measurements of ripples on Ge surfaces after Xe^+ ion beam erosion for different ion energies E_{ion} is given in figure 11 (for details see [34]). The intensity spectra show a multiple of equidistant peaks (up to eighth order) appearing due to the high lateral ordering of ripples. The high intensity of the central peak is a contribution of the specular beam and the diffuse scattering coming from uncorrelated roughness, including short spatial frequency corrugations observed on AFM images. The comparison of the GISAXS measurements reveals a decreasing distance between peaks, i.e. an increase of the ripple wavelength with increasing E_{ion}. The spectra show
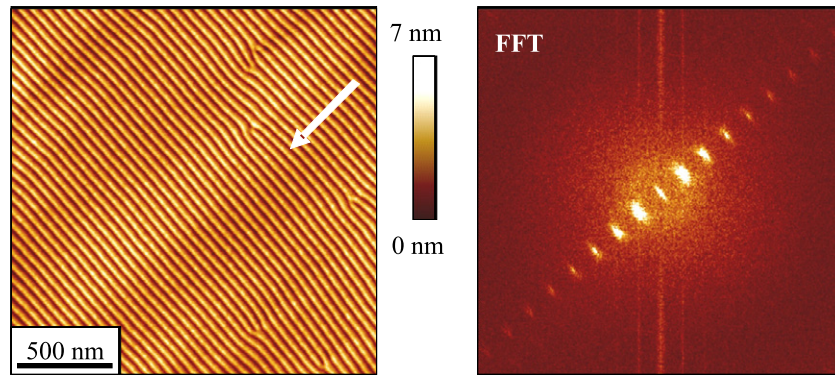
Figure 10. Ripple pattern formation on Si surfaces after Xe$^+$ ion beam erosion at $E_{ion} = 2000$ eV, without sample rotation, at $\alpha_{ion} = 15°$. Also given is the corresponding FFT image.
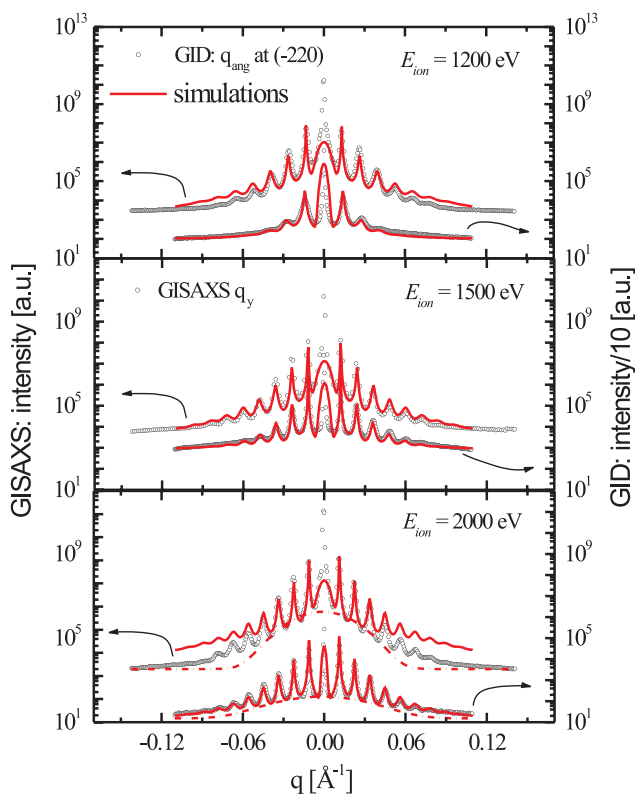

Figure 11. Comparison between GISAXS and angular GID measurements of the ($\bar{2}20$) Ge Bragg reflection for different ion energies. Also given are the simulated curves. The dashed lines (at $E_{ion} = 2000$ eV) indicate the different background intensities of GISAXS and GID.

a slightly better ordering of ripples with increasing E_{ion}. A GID angular scan of samples in the vicinity of the ($\bar{2}20$) Bragg reflection (along the [$\bar{1}$10] crystallographic plane) displays equivalent results compared with GISAXS. This indicates that surface ripples correlate quite well with the crystalline part of ripples. However, in the GID spectra the number of multiple peaks decreases more rapidly with decreasing ion energy compared to GISAXS. This means the crystalline part of ripples at 1200 eV is less ordered compared to the rippled surface. From a comparison of the background intensities

of GISAXS and GID spectra it seems that the a/c interface is more homogeneous compared to the surface (the GISAXS background intensity is higher, as indicated by a more curved form compared to GID: for clarity see the graphs for $E_{ion} = 2000$ eV in figure 11, i.e. the roughness on the surface is higher than on the a/c interface). A summary of inter-peak distances and their widths, deduced from the GISAXS and GID spectra, is given in table 1 (Δq is the distance between peaks). The results show an increase of the ripple wavelength with ion energy for both GISAXS and GID data, similar to AFM results. However, the values deduced from GISAXS are, for principle reasons, about 20% smaller compared to AFM. Further, the peak width δq decreases with ion energy, indicating an improved ordering of ripples with E_{ion}. For comparison the peak width deduced from the PSD spectra, using AFM images, are given. Taking into account the low statistics due to the scan size limit in the AFM data, δq_{PSD} given in table 1 are in the range of δq values from the GISAXS and GID data.

Additional to the experimental data, the corresponding simulated curves are also plotted in figure 11. The simulations are performed using the expressions for the correlation function of the linear paracrystal model and the form factor of a cone, and the assumption that the peaks have a Gaussian distribution [48, 28, 30]. From the simulated curves the model reproduces quite well the distance between peaks as well as the number of multiple peaks. However, with this model the width of the first peak is underestimated by at least an order of magnitude. Probably the short spatial frequency corrugations, the defects of ripples and their asymmetry should be included in the model. Beside this, by analyzing the fitting parameters listed in table 2 the model seems to be a good approximation. Thus, the fitting parameters for the form factor, the radius R_{mean} (base), the height h and the angle γ of the cone correlate very well to the results deduced from AFM and HRTEM images for ripples on Ge. For comparison the mean height deduced from AFM images, h_{AFM}, is also given in table 2.

For the correlation function the wavelength of nanostructures λ (chosen to coincide with the experimental values) and the size deviation σ are used as fitting parameters. By changing the value of the size distribution parameter σ the number of multiple peaks and their intensity vary simultaneously, i.e. they
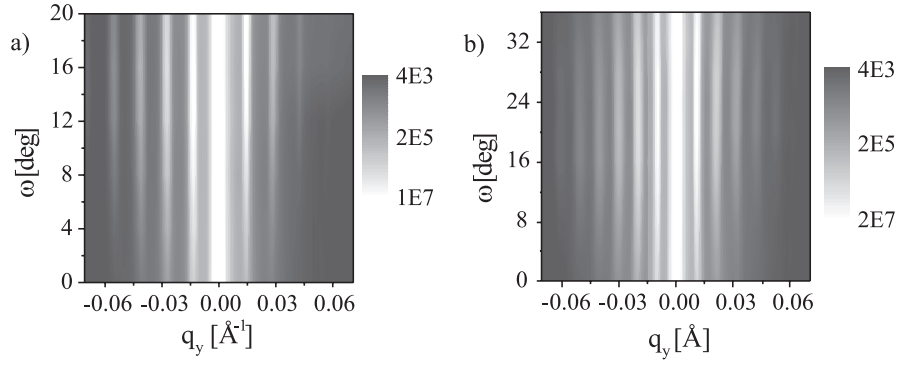
Figure 12. A GISAXS map of ripple Si samples in logarithmic scale sputtered for different ion energies (a) 1200 eV and (b) 2000 eV. The samples are scanned at different azimuth angles ω. The peaks have equidistant spacing with (a) $\Delta q = \pm 0.014$ Å^{-1} and (b) $\Delta q = \pm 0.010$ Å^{-1}. The central peak (white line) in the map is due to the intense diffuse scattering in the plane of incidence at $q = 0$.

Table 1. The inter-peak distances, peak width and the corresponding ripple wavelengths for GISAXS and GID spectra for different samples are given. Also the wavelengths of ripples and the peak width deduced from PSD spectra of AFM images are given for comparison.

E_{ion} (eV)	Δq_y (Å^{-1})	δq_y (Å^{-1})	λ_{GISAXS} (nm)	Δq_{ang} (Å^{-1})	δq_{ang} (Å^{-1})	λ_{GID} (nm)	λ_{AFM} (nm)	δq_{PSD} (Å^{-1})
1200	±0.0127	0.001 86	48	±0.0133	0.003 17	47	56	0.0011
1500	±0.012	0.001 68	52	±0.012	0.001 56	52	63	0.0010
2000	±0.0113	0.001 62	56	±0.0115	0.001 35	55	68	0.001 07

Table 2. The parameters used in the fitting procedure for GISAXS and GID data and the calculated lateral correlation lengths. For comparison the mean height of ripples h_{AFM} deduced from the AFM images is given.

E_{ion} (eV)	λ_s^{GISAXS} (nm)	σ_s^{GISAXS} (nm)	ξ_{GISAXS} (nm)	λ_s^{GID} (nm)	σ_s^{GID} (nm)	ξ_{GISAXS} (nm)	R_{mean} (nm)	γ (deg)	h (nm)	h_{AFM} (nm)
1200	47	3.1	5 600	45	5.1	1 700	15	10	2	2.5
1500	52	2.8	8 600	53	3.7	5 500	15	15	4	3.4
2000	56	2.8	11 200	56	2.8	11 200	20	15	5.3	4.2

Table 3. The distance between peaks Δq and the peak width δq deduced from GISAXS and GID scans are given together with the calculated wavelength of ripples. For comparison the values deduced from the PSD spectra of the AFM images are also given.

E_{ion} (eV)	Δq_{GID} (Å^{-1})	δq_{GID} (Å^{-1})	λ_{GID} (nm)	Δq_y (Å^{-1})	δq_y (Å^{-1})	λ_{GISAXS} (nm)	λ_{AFM} (nm)	δq_{PSD} (Å^{-1})
1200	±0.0142	0.001 49	44	±0.0141	0.001 86	45	47	0.001 61
2000	±0.0103	0.001 46	60	±0.0101	0.001 65	62	64	0.001 67

are related to each other. The size dispersion is in the range between 5% and 7%. With these values, applying the relation $\xi = \lambda^3/2\sigma^2$ from the short-range model (SRO) given earlier, the lateral correlation length ξ is calculated. ξ increases with E_{ion} and can reach up to $\xi = 11.2$ μm for ripples at an ion energy of 2000 eV, which is remarkably high.

Ripples on Si. Figure 12 shows a GISAXS map of ripples on Si for two different ion energies. The samples are sputtered using Ar$^+$ ions at $\alpha_{ion} = 15°$ and $\Phi = 6.7 \times 10^{18}$ cm^{-2}. The scans are recorded for different azimuth angles ω. The order-induced intensity lines along q_y are clearly visible. The number of multiple lines proves the high lateral ordering (alignment) of ripples. The maps indicate an improved ordering of ripples at $E_{ion} = 2000$ eV compared to $E_{ion} = 1200$ eV. Additionally, there is an asymmetry in the intensity distribution and the

number of peaks. This confirms the asymmetric form of ripples similar to the AFM line profiles and HRTEM images [13]. The distance between intensity lines is related to the ripple wavelength by $\lambda_{GISAXS} = 2\pi/\Delta q_y$. A line profile for a particular ω value gives a ripple wavelength of $\lambda = 45$ and 62 nm, respectively. This corresponds quite well with the wavelength deduced from the PSD spectra of AFM images summarized in table 3. From the map the angular distribution of ripples can also be deduced by taking a line profile for a given q_y value, and determine the FWHM of the peak (figure 13).

This is done by making a Gaussian fit to the experimental data. The angular distribution of ripples is 13° for $E_{ion} = 1200$ eV and 19° for $E_{ion} = 2000$ eV. In figure 13 the angular distribution for a sample sputtered for larger fluences is also presented ($\Phi = 1.3 \times 10^{19}$ cm^{-2}, $E_{ion} = 1200$ eV,
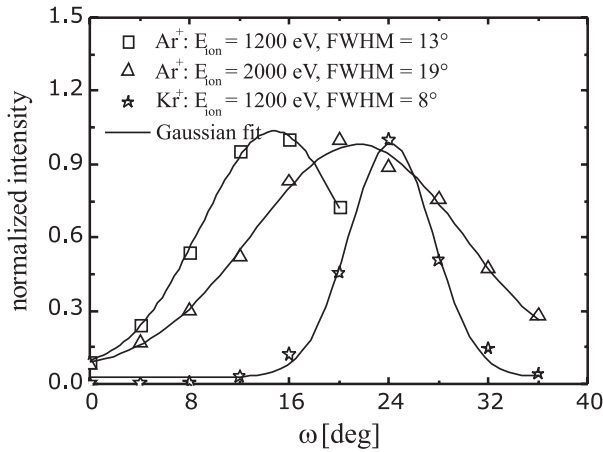
Figure 13. Angular distribution of ripples for samples using (a) and (b) Ar$^+$, and (c) Kr$^+$ ions. The data are taken from GISAXS maps for a given q_y for different azimuth angles ω. The solid lines are a Gaussian fit of the data.

$\alpha_{ion} = 15°$, with Kr$^+$ ions), and is about 8°. A comparison of results indicates that the angular distribution of ripples decreases, i.e. their alignment increases, with ion fluence. From an approach similar to the Ge case, the SRO model can be applied to evaluate the experimental data for Si. From the simulations a lateral correlation of 6250 and 9264 nm is deduced, respectively. Also the form factor fitting parameters have reasonable values compared to the AFM height data. However, the model cannot predict the asymmetry of the experimental data and the width of the first peak is narrower than the experimental one. Probably a model where one can control the inclination angles of the cone independently will be more appropriate. In conclusion the GISAXS and GID measurements show: (i) very good correlation between the surface structures and the a/c interface; (ii) the results correlate very well with the AFM studies; (iii) ripples have a large scale ordering with a correlation length up to 10 μm and (iv) the alignment of ripples increases with ion fluence.

4.2. In situ measurements

The use of *in situ* x-ray scattering to study the formation and stabilization of the different nanostructures *during* the sputtering process is an interesting approach to the understanding of the IBS process. It combines the characteristics of non-destructiveness and high statistical sampling typical for x-rays with the capability of performing *real-time* studies, with a resolution of a few seconds. In this section we discuss some recent results of *in situ* x-ray scattering investigation of nanopatterns during their formation by ion erosion, performed at the beamline ID01 of the ESRF, Grenoble. This approach already used by other groups for the study of IBS on Si [42, 38–40] is here presented for different systems: the formation of dots on GaSb substrates, as a function of ion energy, time and temperature, and the formation of ripples on a Ge(001) substrate as a function of time and energy.

4.2.1. Time evolution of GaSb nanodot patterns at different energies. One of the first investigations of IBS surface nanopatterning by x-ray scattering techniques *in situ* has been performed to study the dot formation on GaSb(001) surfaces [18]. For this study, GISAXS has been used to follow the self-organized patterns forming during Ar$^+$ ion erosion at normal incidence in the ion energy range 300–1200 eV. The main result obtained from this investigation is the increase of pattern wavelength and lateral ordering with sputtering time, with a slower pattern evolution and a higher lateral ordering for lower ion energy. In analogy with the case shown in section 4.1.1, the different timescales for the pattern formation and stabilization at different energies are attributed to the different values of the sputtering rate.

The GaSb(001) surfaces were irradiated with Ar$^+$ ions at three different energies (300, 700 and 1200 eV) under normal incidence. The ion current density was 100 μA cm^{-2} except for the low energy value, which was approximately half. Due to the absence of the cooling system at that time, the sample temperature during ion erosion increased up to 80 °C. Erosion and GISAXS measurements were done sequentially, interrupting the erosion process before each measurement. The x-ray beam had a wavelength of 1.54 Å at an incidence angle $\alpha_i = \alpha_c^{GaSb} = 0.25°$. The scans were recorded with a linear position-sensitive detector placed perpendicular to the sample surface. The signal was integrated along the detector in an α_f range of about 2° above the sample surface. In this way, a sequence of GISAXS profiles were recorded successively to follow the surface lateral morphology, with no information on the perpendicular direction (we posed the emphasis on the lateral morphology disregarding the information on the dot height along the surface normal). The first appearance of the correlation peaks in the GISAXS scans reveals the time threshold for the pattern formation. Afterward, the evolution of the surface pattern can be followed by monitoring the changes in the correlation peaks position and width in time. From figure 14(a), where the time evolution of the GISAXS spectra measured sequentially during ion bombardment at 700 eV is shown, one can see that the pattern formation starts already during the first minute. The coarsening of the pattern is then clearly shown by the shift of the correlation peaks towards smaller $|Q_y|$ values. Finally, the increase of the intensity and the narrowing of the correlation peaks reveal the enhancement of ξ driven by self-organization.

The model used to fit the GISAXS scans (see figure 14(c)) is the isotropic two-dimensional hexagonal paracrystal model [49, 30], where the hexagonal packing of the nanodots is only local and described by ξ. The fitting results for λ and the normalized correlation length ξ/λ are plotted in figure 14(b) upper and lower panel, respectively. Similar trends are found for the different ion energies, i.e. the patterns appear after an irradiation time of a few minutes, and λ increases with time until reaching a saturation value that scales with ion energy.

Even if the increase of λ with time is quite small (15%), it can be resolved unambiguously. Most interestingly, this coarsening mechanism is accounted for by the recently proposed hydrodynamic model for pattern formation during IBS, and had not been observed before on GaSb surfaces [50, 46]. We
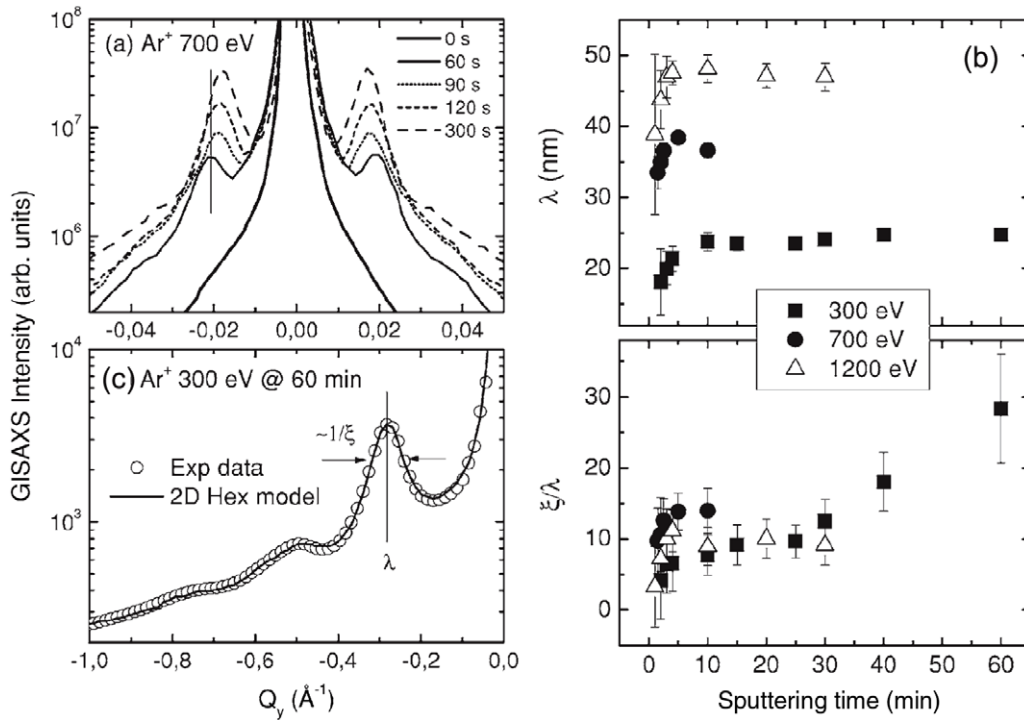
Figure 14. (a) GISAXS scans showing the temporal evolution of nanodot pattern formation on GaSb(001) by IBS under 700 eV Ar$^+$. (b) Temporal evolution of the wavelength λ (top) and normalized correlation length ξ/λ (bottom) for nanodot patterns at different ion energies. (c) Fit of the GISAXS intensity (GaSb sputtered at 300 eV for 60 min) to the 2D hexagonal paracrystal model [18]. Reprinted with permission from [18]. Copyright 2007, American Institute of Physics.

attribute the disagreement with previous studies performed on GaSb by AFM [36] to two main reasons. On the one hand, the higher resolution and better sampling statistics of the GISAXS technique. On the other, the use of an appropriate model to interpret the GISAXS data is a better approach and provides more accurate results than the Gaussian fit of the PDS of the AFM data. The second important result is the slower time evolution, together with the achievement of a higher degree of ordering, for lower ion energy, as shown in figure 14(b). To explain this trend we recall that changing the ion energy results in a different sputtering rate (SR). At 1200 eV it is nearly four times larger than at 300 eV, as derived from the calculated sputtering yield by the SRIM [51] code and the measured sample current density. In analogy with the results reported for Si nanodots in section 4.1.1, and in agreement with predictions from the hydrodynamic model, a faster time evolution is expected for higher SR, while the lower SR results in a larger correlation length.

4.2.2. Early-time behavior of nanodot formation on GaSb at normal Ar$^+$ ion erosion. This study is motivated by previous results showing evidence of a transient morphology in the early stage of erosion of Ge surfaces during Xe IBS in off-normal conditions (cf section 4.1.3). Here we follow *in situ* the first moments of the sputtering process on a GaSb surface during Ar$^+$ ion erosion at normal incidence [52]. In contrast to earlier investigations of the roughening behavior of ion-eroded GaSb surfaces [36], performed *ex situ* with the AFM technique, where only an increase in the roughness had been measured, here we observe a transient smoothing of the surface that

precedes the roughening regime and the successive nanodot formation.

The experimental set-up used is the same as described in the previous section. As for the previous case, measurements were performed sequentially, after consecutive steps of short exposures of the sample surface to the ion beam. The GaSb(001) surfaces were eroded with Ar$^+$ ions at normal incidence with an energy of 450 eV, with a low ion current at the sample, corresponding to an ion flux of 1×10^{15} cm^{-2} s^{-1}. The sample temperature did not increase above 60 °C during the sputtering steps. With respect to the measurements described in the previous section, performed at time intervals of about 60 s, the sequential sputtering was performed here with lower current density and for shorter periods (namely every 10–20 s of erosion), allowing a finer sampling of the surface morphology versus time and ion dose. The transient smoothing and the successive roughening regime were monitored by a combination of x-ray reflectivity and GISAXS measurements, which give complementary information on the surface morphology. The intensity of the x-ray reflectivity from a surface decreases for increasing roughness while, in the same conditions, the roughness-induced diffuse scattering around the specular beam (i.e. the GISAXS signal) increases. The comparison of these two measurements provides a good measure of the roughness evolution of the investigated surface. Figure 15 shows the results of these investigations. The increase of the reflectivity for ion dose up to a value of 1.4×10^{17} cm^{-2} and the corresponding decrease of the diffuse intensity around the specular beam in the GISAXS pattern (not shown here)
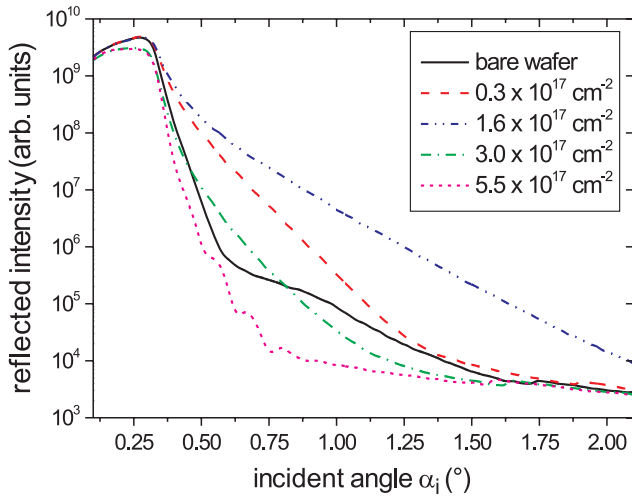
Figure 15. Reflectivity measurements obtained at different stages during the erosion of a GaSb surface by 450 eV Ar$^+$ ions. The initial smoothening is evident from the strong increase in reflectivity, whereas the following pattern formation at larger fluence is accompanied by a strong surface roughening.

indicate a smoothening of the GaSb surface during the first moments of the ion erosion process. For higher ion dose, a set of correlation peaks appears in the GISAXS signal, a typical signature of the onset of correlated structures on the surface. At the same time, a strong reduction of the surface reflectivity indicates a sudden increase of the surface roughness, accounted for by the formation of the nanodot pattern. The coarsening of the dot pattern is confirmed by the further decrease in the reflected intensity and the appearance of thickness oscillations in the reflectivity curve, indicating the formation of a surface layer with a density different from the starting surface, and the underlying substrate. The thickness and the density of this surface layer are consistent with the presence of a dot pattern forming on the surface nanopattern. This regime of surface smoothing has the same origin as the relaxation mechanism for the formation of periodic structures, supported by results from simulations done using a continuum equation. Details of this on-going work will be given elsewhere [52].

4.2.3. Temperature dependence of the surface morphology of GaSb(001) during normal Ar$^+$ ion erosion. This study was intended to investigate, *in situ*, the role of the thermally induced surface diffusion on the nanopattern formation during IBS. To this end, we performed *in situ* GISAXS measurements during the erosion of GaSb at different temperatures of the substrate. The GaSb(001) surfaces were eroded at normal incidence by Ar$^+$ Ions at an energy of $E = 500$ eV in a wide temperature range, $T = [150–500]\,°C$ [53]. In these conditions an ordered pattern of dots is expected for low temperatures.

In this experiment the GISAXS profiles were recorded during the sputtering process in a continuous mode, with no interruption of the erosion process. In order to achieve the necessary time resolution for this type of measurement, the spectra were acquired by a linear detector mounted parallel to the sample surface. In this way we could measure the
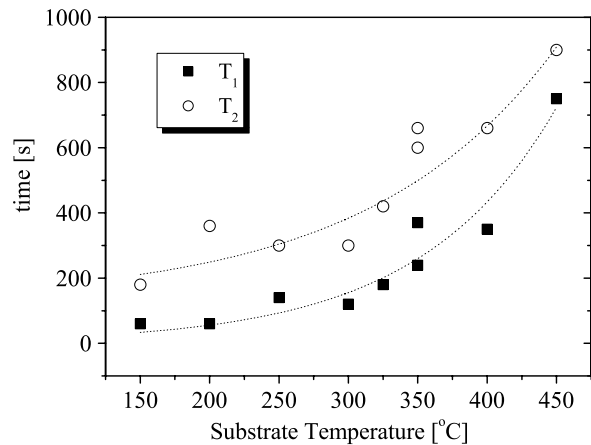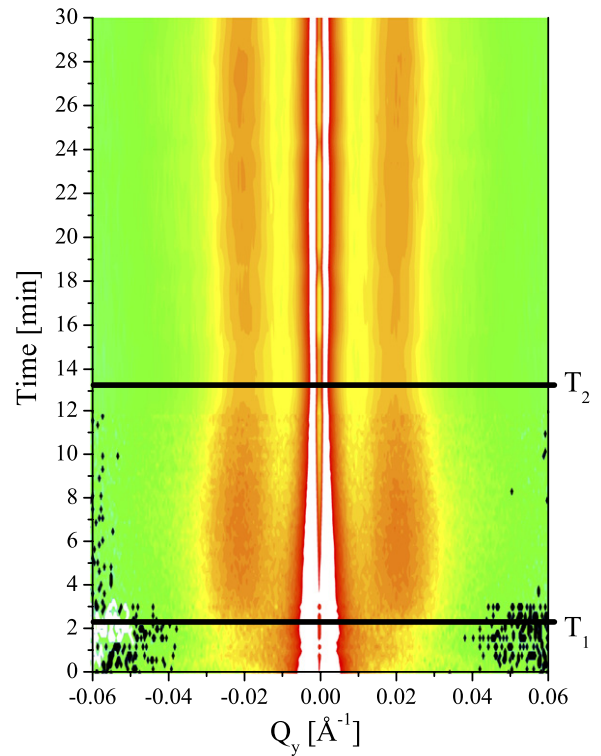

Figure 16. (Top) GISAXS–time map for GaSb surface eroded at 500 eV at $T = 250\,°C$. The onset of the self-organized nanodots is evident from the appearance of the correlation peaks. (Bottom) Temperature dependence of the onset and stabilization of the nanostructures.

whole GISAXS pattern at each acquisition, i.e. within 2–3 s, without movement of the detector arm. Doing so, we obtained 2D maps of the GISAXS pattern versus time, as the one shown in figure 16 (top). The measurements were performed with an integration time of 10″ for the first 10 min of sputtering (where the nanopatterns are expected to appear) and an integration time of 60″ for the rest of the time (where the pattern stabilization should occur). The total time of sputtering was fixed at ∼30 min, based on measurements performed at room temperature, for which this time was enough for the patterns to form and stabilize.

This experiment shows that the kinetics of the formation of the nanopatterns has a marked dependence on the substrate

temperature: the characteristic time for the formation of the patterns and the time needed for the structures to stabilize increase with increasing temperature, as summarized in figure 16 (bottom). We attribute this behavior to the increased mobility of the surface atoms, which might compete with the self-organized process of formation of an ordered pattern. Furthermore, the ordering of the nanopattern is better for 'low' substrate temperatures. This is seen from the amplitude of the ordering peaks in the GISAXS spectra, as well as from the appearance of second-order peaks. The best ordered patterns are obtained for temperatures below 300 °C. In these conditions, the intensity of the ordering peaks has a clear onset at a time T_1, then it saturates (T_2) and stays constant until the end of the IBS process. Moreover, during the IBS process, the characteristic wavelength of the dot pattern, which is in the range of 20–30 nm, evolves, slightly increasing with time, and the correlation length improves (appearance of second-order SL peaks), in agreement with our previous measurements. For samples with $T_{sub} > 300$ °C the onset of the dot correlation occurs at later times, and the intensity of the SL peaks decreases after a characteristic time t_{dec}, which also depends on the temperature. Finally, the coarsening of the structures is stronger for low temperatures.

AFM measurements confirm that the final morphology of the nanopatterned surfaces shows a marked sensitivity on the substrate temperature. The average interdot distance for temperatures below 300 °C varies in the range 20–30 nm and increases with temperature. Above 300 °C this distance rapidly increases in the range 30–60 nm. The roughness, as measured from AFM analysis, increases exponentially with T. For temperatures $T > 400$ °C GISAXS spectra do not show evidence of pattern formation, but indicate the development of a strong surface roughness. This is confirmed by AFM measurements, which indicate roughness of the order of a few hundred nm. The driving force for this could be a preferential sputtering of one element with respect to the other in the GaSb compound, which could change the properties of the surface during the erosion process and induce a change in the kinetics of the nanopattern formation. Confirmation of the preferential sputtering model is still lacking and can be expected from combining strain-sensitive GID with chemically sensitive anomalous scattering at the Sb K edge. Details of this work will be given elsewhere [53].

4.2.4. Time evolution of ripple morphology on Ge surfaces by off-normal IBS. We studied the onset and time evolution of ripple patterns formed during erosion of Ge(001) surfaces by Xe$^+$ ion beams at off-normal incidence and at two different energies. The morphology of the Ge surfaces during ion erosion was investigated *in situ* by grazing incidence small-angle scattering (GISAXS).

Nanostructures in the shape of dots and ripples have been produced on Ge(001) surfaces using a Xe$^+$ ion beam at two energies, 1000 and 500 eV, at a controlled substrate temperature $T = 35(\pm 1)$ °C. The initial surface of the substrate has a root mean square roughness rms $\leqslant 0.3$ nm. The ion beam current density used for all the samples was 55 μA cm^{-2}, providing an ion flux of 3.4×10^{14} s^{-1} cm^{-2}.

In order to carry out GISAXS measurements on ripples during ion erosion at off-normal incidence, the HV chamber had to be tilted by an angle $\delta = -\theta_{ion}$ on the sample stage, in order to recover the alignment of the sample surface with respect to the incident x-ray beam, required for the measurements. Measurements were performed at an incident angle $\alpha_i = 0.3°$ slightly larger than the critical angle for x-ray total external reflection, which for Ge at this wavelength is $\alpha_c = 0.275°$. Data were acquired by a linear position-sensitive detector parallel to the sample surface, as for the previous examples, positioned at a fixed exit angle $\alpha_f = 0.4°$. A beam stop placed at the position of the plane of incidence prevents detector saturation. The output of such measurements (not shown here) are 'time–GISAXS' maps, similar to the one shown in figure 16, displaying the variation of the signal coming from the nanostructuring process of the Ge surface as a function of time.

Summarizing, for Xe$^+$ ion beam erosion at $\theta_{ion} = 10°$, ripples are formed within a few minutes from the start of the IBS process for the two energies explored. Stabilization of the lateral periodicity λ occurs for long erosion time at both energies. Increase of the lateral ordering ξ also occurs during the IBS process, which does not reach saturation within the explored time range. Comparing the results obtained, we observe that the correlation length and the ripple alignment are better for Xe$^+$ at 1 keV. AFM images confirm the results obtained with x-ray scattering measurements, and indicate that, for samples eroded with a 500 eV beam, the ripples are shorter and less ordered than in the case of 1 keV Xe$^+$ beam erosion. Moreover, in the latter case the presence of dots that break the continuity of the ripples is observed, which is not observed in the case of the 500 eV sample. This transition from dot to ripples has been observed and reported in a previous publication [33]. The main observation was that ripples are obtained by merging of dots which are formed in the first minutes of sputtering. This does not seem to be the case for 500 eV samples.

5. Results: medium energy IBS

In this section, we focus on the investigation of ripples produced by medium energy Xe$^+$ (5–35 keV) and Ar$^+$ (60–100 keV) ion beam sputtering on Si(001) surfaces. In this energy range, ripples are usually observed for incidence angles of the ion beam between 50° and 80° off-normal. Wavelength and quality of the ripple patterns can be controlled by varying both the ion incidence angle and the ion energy. By this, the wavelength can be tuned between 50 nm for 5 keV Xe$^+$ bombardment up to 1000 nm, if 100 keV Ar$^+$ ions are used. For details about the sample preparation see [54, 55]. However, there is a distinct difference in using medium to high energetic ions compared to the use of low energetic ions as described in the previous sections. Ions with energies up to 2 keV, as available from most of the broad-beam ion sources and widely exploited in many experiments, usually create a patterned surface covered by a thin amorphous layer, usually of the order of 2–10 nm thick. For energies up to 100 keV, and especially in the case of light ions like argon, the thickness of
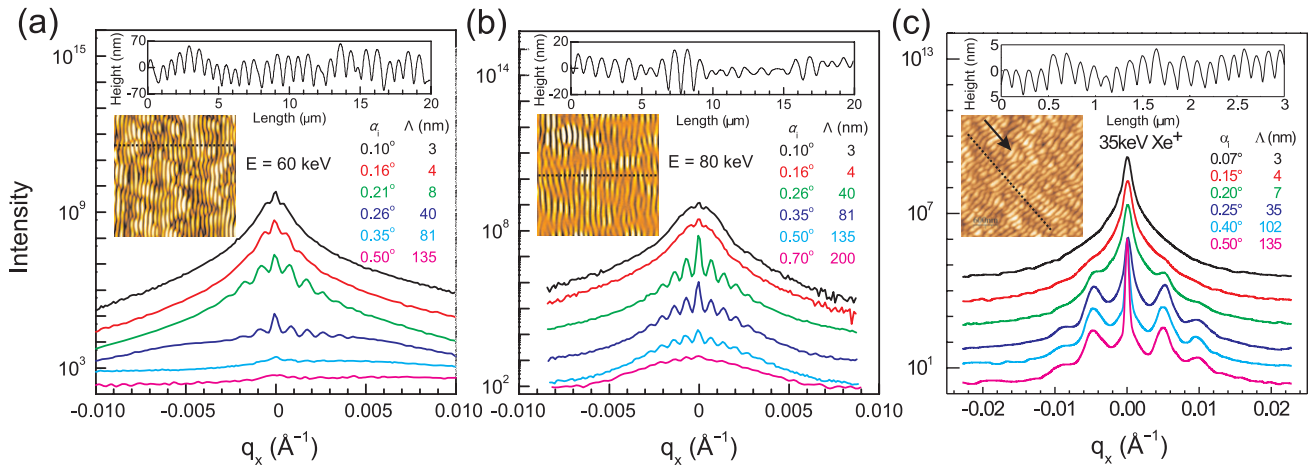
Figure 17. (a), (b) Transverse GID curves around the (220) Bragg peak of Si(001) for different angles of incidence (α_i), i.e. x-ray penetration depth Λ, and Ar$^+$ ion energies of 60 and 80 keV. In each panel, curves are shifted vertically for clarity. Insets: corresponding typical AFM images (size 20 μm × 20 μm) and horizontal line profiles through the AFM images, indicating the typical height variation in each sample. (c) Corresponding measurements of a sample irradiated by 35 keV Xe$^+$ ions. The size of the AFM image is 3 μm × 3 μm. Reproduced with permission from [54]. Copyright 2004 by the American Physical Society.

this amorphous layer can become considerably larger, e.g. up to several hundred nm. This amorphous layer is typically followed by a transition region to the crystalline part which shows ripple formation as found at the surface. To be able to study both the surface morphology as well as the morphology of the amorphous–crystalline (a/c) interface located several hundred nm below the surface with good statistical sampling, the techniques of GID and GISAXS are mostly suitable. In addition, this near-surface-sensitive techniques allow us also to study the structure of the amorphous region [56].

In order to study the evolution of the buried a/c interface, GID was performed, varying the incidence angle α_i with respect to the sample surface and therefore the penetration depth of the probing x-ray beam in the sample. Typical AFM images for Ar$^+$ sputtered Si surfaces and corresponding GID curves for different incidence angles are shown in figures 17(a) and (b).

The GID transverse q_x curves for the ion-bombarded samples show the presence of satellite peaks on both sides of the main (220) Bragg peak. The appearance of satellite peaks must be originated by a lateral undulation of the crystalline part of the sample. As seen in figure 17, the presence of satellite peaks in q_x scans is prominent after certain values of α_i, which indicates that the ripple-like modulation of crystalline materials is present only below a certain depth from the top surface. Values for the penetration depth Λ corresponding to the value of α_i are indicated in figure 17 and have been calculated considering the values of the critical angle α_c and the absorption coefficient μ for perfect Si. For very low α_i no satellite peaks were found, which indicates the absence of lateral correlation of the material in the top layer. However, a distinct but broad Bragg peak can be observed, indicating the existence of remaining crystalline material. With increasing α_i the number of grating peaks increases, reflecting the increasing correlation of ripples in the crystalline material. At a certain value of α_i the shape of the curve changes from a narrow to a broad one, indicating the onset of defect formation. The depth

of this transition is obviously related to the penetration depth of the implanted ions, which increases with the increase of ion energy, E, due to a reduced interaction of the implanted ions with the host lattice as predicted from the stopping and range of ions in matter (SRIM) calculation [51]. This finding corresponds to the decrease of ripple height (amplitude) with the increase of E. Figure 17(c) shows transverse GID scans for a sample irradiated with 35 keV Xe$^+$ ions. Although qualitatively similar, the amplitude of the ripples and correlation length are considerably smaller in this system as only two satellite peaks are visible.

Besides studying the wavelength at the a/c interface, the absolute intensity of the Bragg peak as a function of the incidence angle (α_i scan, also referred to as the Vineyard profile [57]), is related to the density of crystalline material in the depth corresponding to the actual incidence angle. Measurement of these α_i scans can therefore be used to obtain information about the degree of crystallinity of the surface region affected by the ion bombardment.

Vineyard profiles for samples bombarded with different doses are shown in figure 18. Such α_i scans are very much different from a typical shape, where a single peak is observed at $\alpha_i = \alpha_c$ (see the dashed line in figure 18(b)). Instead, for the present samples, one observed an additional hump (plateau) starting at around $\alpha_i = 0.02°$. This corresponds to material of low but gradually decreasing density. However, since the measurements are performed in the vicinity of an in-plane Bragg peak, the intensities correspond to the density of crystalline materials. The position of these peaks, and the plateau in between, represent the total density of silicon having dispersed crystallites as a function of depth. It can be noted that the onset angle of the plateau, the shape and height of the plateau, and α_c are all functions of implantation dose. For low doses there are two distinct critical angles: the appearance of a peak at $\alpha_i < 0.05°$ corresponds to the existence of a partial crystalline top layer with a much lower density compared to that of crystalline silicon (α_c).
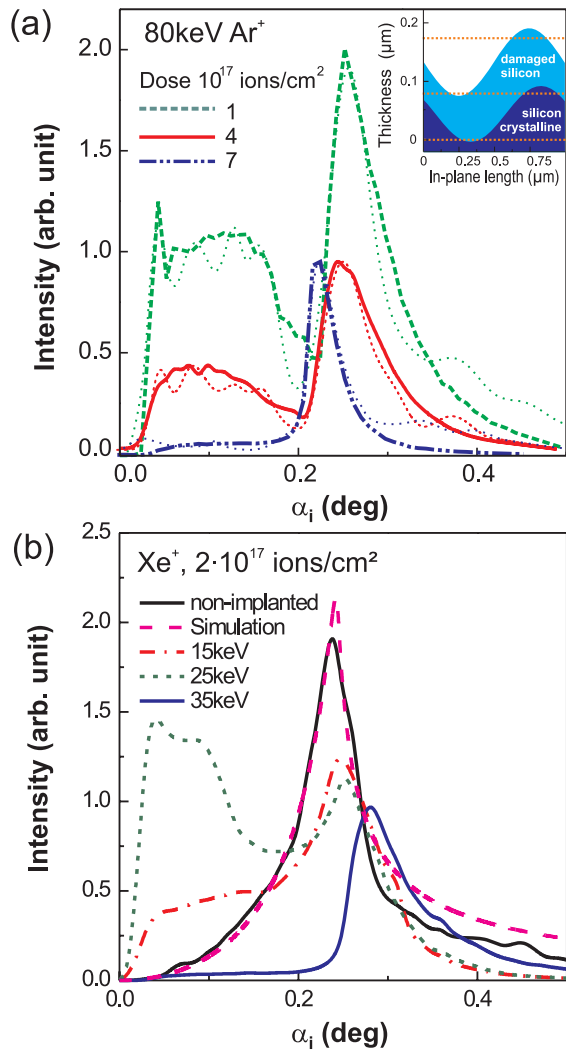
Figure 18. (a) Experimental and simulated (dotted) α_i scans of samples measured at the (220) Bragg peak of Si(001) substrate irradiated with Ar$^+$ ions and different dose at ion energy $E = 80$ keV. The inset shows a schematic side view of the sample used for the depth profile calculation. (b) α_i scans of samples irradiated with Xe$^+$ ions of different energy and fluence 2×10^{17} ions cm^{-2}. Reproduced with permission from [54]. Copyright 2004 by the American Physical Society.

This behavior was first observed in the case of Ar$^+$ sputtered surfaces as a function of ion fluence (figure 18(a)). For increasing fluence the intensity of the plateau region decreases. In the case of a fluence of 7×10^{17} ions cm^{-2}, the plateau region almost disappears and the shape of the α_i scan curve corresponds to a typical Vineyard profile through a 'dead' (amorphous) top layer [57]. By assuming a gradual decrease of the (crystalline) Si density that stems from the damage and the periodic modulation of the surface region, it is possible to simulate the scattering intensity of the Vineyard profiles (dotted lines in figure 18(a)) and to retrieve the vertical density profile of crystalline silicon [54]. In the case of Xe$^+$ sputtering, the same trend could be observed as a function of ion energy (figure 18(b)): starting from a non-sputtered sample that shows the typical Vineyard profile, a plateau region of increasing intensity is observed for ion energies up to 25 keV.

However, when the energy is further increased to 35 keV and beyond, the plateau vanishes and only the signature of a complete amorphous layer is observed.

Besides studying the morphology of the a/c interface, we applied GISAXS to compare shape and ordering of the surface and a/c interface [55]. As an example, figure 19(a) shows GISAXS measurements of a sample irradiated with 15 keV Xe$^+$ ions under 70° off-normal incidence and a total fluence of 2×10^{17} ions cm^{-2}. The map was recorded using a one-dimensional position-sensitive detector (PSD) placed perpendicular to the surface, allowing us to record two-dimensional slices through reciprocal space by scanning the in-plane scattering angle 2θ, i.e. equivalent to the usage of a two-dimensional detector as illustrated in the inset in figure 19(c). The specular reflected beam in the center is surrounded by diffuse scattered intensity, showing asymmetric streaks and superimposed satellite peaks. The asymmetric intensity distribution can be attributed to an asymmetric shape of the surface ripples, whereas the position and width of the satellite peaks are related to the mean wavelength λ and correlation length ξ of the surface structure [28].

For a quantitative analysis, line sections of the GISAXS profiles have been extracted and fitted using the program *IsGISAXS* [30]. To simulate asymmetrically shaped ripples, we used the form factor of asymmetric truncated pyramids as shown in the inset in figure 19(c). The one-dimensional paracrystal model [49] was used to extract the information about the mean wavelength and correlation length. As an example, figure 19(c) shows the results of the fits along the lines indicated in figure 19(a).

The GISAXS measurements can be directly compared with transverse GID scans, which probe only the crystalline part of the sample and therefore the morphology of the buried a/c interface. Figure 19(b) shows an example of such a scan, taken at the same sample at incidence angle close above α_c. The intensity distribution shows excellent agreement with the corresponding GISAXS measurement. The accordance holds for both the overall shape of the pattern as well as the width and relative intensities of the satellite peaks. Because GISAXS is only sensitive to the morphology of the amorphous near-surface layer and GID to the crystalline substrate, one can deduce that both surface and interface show the same morphology with a comparable degree of ordering.

Figure 20 summarizes the results of the GISAXS and GID analysis for the investigated Xe$^+$ implanted samples, showing the evolution of wavelength and order parameters vs. ion energy. In the investigated energy range, the wavelength increases almost linearly with ion energy ($\lambda \sim E$) for 65° incidence, whereas the evolution follows a power law for 70° incidence ($\lambda \sim E^{0.5}$). In both cases, the increase in wavelength is accompanied by a small decrease in normalized correlation length, i.e. the mean number of ordered ripples decreases. The absolute value of the correlation length increases from 1 μm (5 keV) towards 2.5 μm (35 keV). In the case of Ar$^+$ sputtering under 60° off-normal incidence, the wavelength was found to increase almost linearly from 720 nm at 60 keV up to 1080 m at 100 keV.

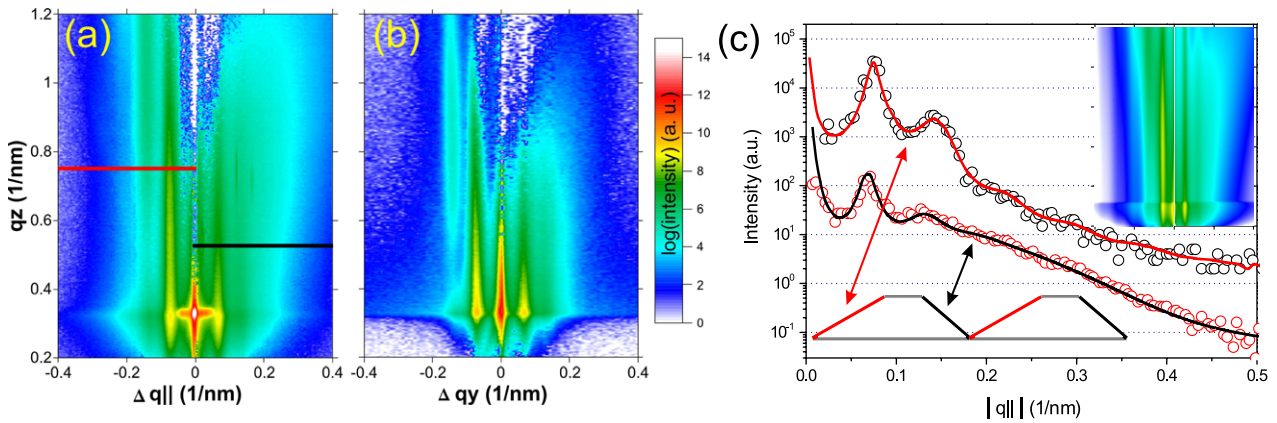In summary, we have applied the techniques of GID and GISAXS to study the structure and morphology of ripple

Figure 19. (a) GISAXS measurement of a sample irradiated with 15 keV Xe$^+$ ions under 70° incidence angle. Visible are satellite maxima and an asymmetric intensity distribution caused by the asymmetric shape of the ripples. (b) GID measurement of the same sample. Good agreement with (a) indicating similar shape and ordering of surface and a/c interface. (c) Simulations (lines) of the GISAXS intensities along the lines indicated in (a) (circles). Adapted from [55]. Copyright 2008, American Institute of Physics.
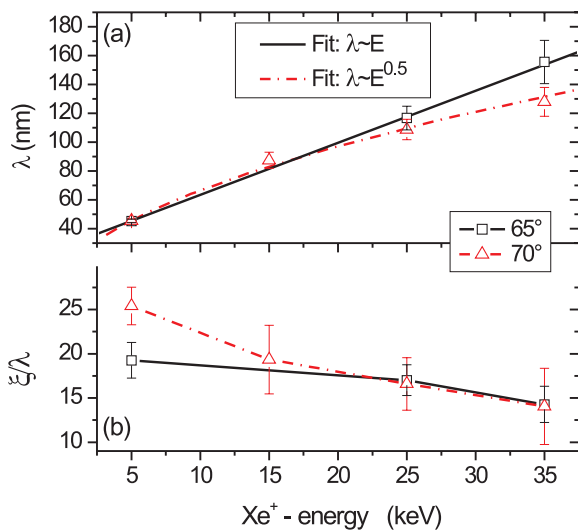
Figure 20. Energy dependence of (a) the wavelength λ and (b) the normalized correlation length ξ/λ for Xe$^+$-induced ripples as obtained from the GISAXS analysis. Adapted from [55]. Copyright 2008, American Institute of Physics.

patterns produced by medium energy Ar$^+$ and Xe$^+$ off-normal irradiation of Si(001) surfaces. The combined use of these techniques allows us to investigate and compare the morphology of both the surface and the a/c interface. In addition, the characteristic intensity profile of the Bragg peak as a function of x-ray penetration depth can be used to retrieve information about the vertical density profile of crystalline material and obtain information about the degree of amorphization.

6. Conclusion and outlook

In this paper we have demonstrated the advantages of using grazing incidence x-ray scattering techniques to study nanopattern formation on semiconductor surfaces due to ion beam sputtering. The results cover a wide parameter field of IBS, ranging from low to medium ion energy, normal and off-normal incident sputtering angles, *ex situ* and *in situ*

experiments, different materials, etc. Nevertheless, new questions are evolving from this work, which can especially be addressed by extending the x-ray techniques presented here. One issue is the strain, evolving during IBS, to which GID is especially sensitive. It turns out that strain seems to be created by the sputtering procedure mainly in bi-elemental semiconductor compounds, like GaSb and InSb. The origin of strain may be caused by preferential sputtering and the corresponding creation of vacancies in one of the sub-lattices. The element-sensitive anomalous GID at the K edge of one or both elements constituting the compound is a promising approach to shed more light on this problem. The theoretical explanation of the strain influence on the pattern formation, lacking so far in the literature, needs to be addressed too.

The experimental set-up for *in situ* x-ray investigations during IBS presented in this paper offers the possibility to study the dot and ripple formation process by the technique of x-ray photon correlation spectroscopy (XPCS), in which the coherence of the x-rays is exploited [58]. This technique could contribute to the understanding of the underlying dynamic processes, leading to the improvement of the ordering of the nanostructures during IBS. We have shown in this paper that the timescale involved reaches some tens of minutes and is thus readily accessible by XPCS. Very recently, XPCS studies have been performed on a GaSb system during Ar$^+$ ion erosion, and their analysis is in progress [59].

Finally, IBS can be applied for creating magnetic nanodots consisting of a sequence of magnetic and nonmagnetic materials. The perfect lateral ordering that evolves during IBS is induced by templating the multilayers with combined techniques [60]. We like to emphasize that the combination of x-ray techniques and IBS remains a unique tool for the production and characterization of self-organized nanostructures with promising perspectives in device applications based on nanotechnology.

Acknowledgments

References

[1] Chan W L and Chason E 2007 *J. Appl. Phys.* **101** 121301
[2] Hofer C, Abermann S, Teichert C, Bobek T, Kurz H, Lyutovich K and Kasper E 2004 *Nucl. Instrum. Methods Phys. Res.* B **216** 178–84
[3] Toma A, Buatier de Mongeot F, Buzio R, Firpo G, Bhattacharyya S, Boragno C and Valbusa U 2005 *Nucl. Instrum. Methods Phys. Res.* B **230** 551–4
[4] Valbusa U, Boragno C and de Mongeot F B 2002 *J. Phys.: Condens. Matter* **14** 8153–75
[5] Aste T and Valbusa U 2005 *New J. Phys.* **7** 122
[6] Navez M, Sella C and Chaperot D 1962 *C. R. Acad. Sci.* **254** 240
[7] Barber D J, Frank F C, Moss M, Steeds J W and Tsong I S T 1973 *J. Mater. Sci.* **8** 1030–40
[8] Carter G, Navinsek B and Whitton L 1991 *Sputtering by Particle Bombardment II* (*Topics of Applied Physics* vol 64) (Berlin: Springer)
[9] Karen A, Nakagawa Y, Hatada M, Okuno K, Soeda F and Ishitani A 1995 *Surf. Interface Anal.* **23** 506–13
[10] Stevie F, Kahora P, Simons D and Chi P 1988 *J. Vac. Sci. Technol.* A **6** 76–80
[11] Vajo J J, Doty R E and Cirlin E H 1996 *J. Vac. Sci. Technol.* A **14** 2709–20
[12] Ziberi B, Frost F, Tartz M, Neumann H and Rauschenbach B 2008 *Appl. Phys. Lett.* **92** 063102
[13] Ziberi B, Frost F, Hoche T and Rauschenbach B 2005 *Phys. Rev.* B **72** 235310
[14] Carter G and Vishnyakov V 1996 *Phys. Rev.* B **54** 17647–53
[15] Brown A D and Erlebacher J 2005 *Phys. Rev.* B **72** 075350
[16] Facsko S, Dekorsy T, Koerdt C, Trappe C, Kurz H, Vogt A and Hartnagel H L 1999 *Science* **285** 1551–3
[17] Frost F, Schindler A and Bigl F 2000 *Phys. Rev. Lett.* **85** 4116–9
[18] Plantevin O, Gago R, Vazquez L, Biermanns A and Metzger T H 2007 *Appl. Phys. Lett.* **91** 113105
[19] Gago R, Vazquez L, Cuerno R, Varela M, Ballesteros C and Albella J M 2001 *Appl. Phys. Lett.* **78** 3316–8
[20] Bradley R M and Harper J M E 1988 *J. Vac. Sci. Technol.* A **6** 2390–5
[21] Sigmund P 1969 *Phys. Rev.* **184** 383–416
[22] Kuramoto Y and Tsuzuki T 1976 *Prog. Theor. Phys.* **55** 356–69
[23] Makeev M A, Cuerno R and Barabasi A-L 2002 *Nucl. Instrum. Methods Phys. Res.* B **197** 185–227
[24] Dosch H 1992 *Critical Phenomena at Surfaces and Interfaces. Evanescent X-Ray and Neutron Scattering: Evanescent X-Ray and Neutron Scattering* (*Springer Tracts in Modern Physics*) (Berlin: Springer)
[25] Warrenca B E 1990 *X-Ray Diffraction* (New York: Dover)
[26] ID01-homepage http://www.esrf.eu/UsersAndScience/Experiments/SurfaceScience/ID01/
[27] Carbone D, Plantevin O, Gago R, Mocuta C, Bikondoa O, Alija A, Petit L, Djazuli H and Metzger T H 2008 *J. Synchrotron Radiat.* **15** 414–9
[28] Schmidbauer M 2004 *X-Ray Diffuse Scattering from Self-Organized Mesoscopic Semiconductor Structures* (*Springer Tracts in Modern Physics*) (Berlin: Springer)
[29] Rauscher M, Paniago R, Metzger H, Kovats Z, Domke J, Peisl J, Pfannes H-D, Schulze J and Eisele I 1999 *J. Appl. Phys.* **86** 6763–9
[30] Lazzari R 2002 *J. Appl. Crystallogr.* **35** 406–21
[31] Gago R, Vazquez L, Plantevin O, Metzger T H, Munoz-Garcia J, Cuerno R and Castro M 2006 *Appl. Phys. Lett.* **89** 233101
[32] Gago R, Vazquez L, Plantevin O, Sanchez-Garcia J A, Varela M, Ballesteros M C, Albella J M and Metzger T H 2006 *Phys. Rev.* B **73** 155414
[33] Carbone D, Alija A, Plantevin O, Gago R, Facsko S and Metzger T H 2008 *Nanotechnology* **19** 035304
[34] Ziberi B, Cornejo F, Frost F and Rauschenbach B 2009 *J. Phys.: Condens. Matter* **21** 224003
[35] Metzger T H, Kegel I, Paniago R and Peisl J 1999 *J. Phys. D: Appl. Phys.* **32** A202–7
[36] Bobek T, Facsko S, Kurz H, Dekorsy T, Xu M and Teichert C 2003 *Phys. Rev.* B **68** 085324
[37] Tan S K and Wee A T S 2006 *J. Vac. Sci. Technol.* B **24** 1444–8
[38] Ozaydin G, Ozcan A S, Wang Y Y, Ludwig K F, Zhou H, Headrick R L and Siddons D P 2005 *Appl. Phys. Lett.* **87** 163104
[39] Ozaydin G, Ozcan A S, Wang Y, Ludwig K F Jr, Zhou H and Headrick R L 2007 *Nucl. Instrum. Methods Phys. Res.* B **264** 47–54
[40] Ludwig F Jr, Eddy C R Jr, Malis O and Headrick R L 2002 *Appl. Phys. Lett.* **81** 2770–2
[41] Sánchez-García J A, Vázquez L, Gago R, Redondo-Cubero A, Albella J M and Czigány Z 2008 *Nanotechnology* **19** 355306
[42] Ozaydin G, Ludwig K F Jr, Zhou H, Zhou L and Headrick R L 2008 *J. Appl. Phys.* **103** 033512
[43] Facsko S, Kurz H and Dekorsy T 2001 *Phys. Rev.* B **63** 165329
[44] Makeev M A and Barabasi A L 1997 *Appl. Phys. Lett.* **71** 2800–2
[45] Frost F, Ziberi B, Hoche T and Rauschenbach B 2004 *Nucl. Instrum. Methods Phys. Res.* B **216** 9–19
[46] Munoz-Garcia J, Castro M and Cuerno R 2006 *Phys. Rev. Lett.* **96** 086101
[47] Yewande E O, Hartmann A K and Kree R 2005 *Phys. Rev.* B **71** 195405
[48] Kegel I, Metzger T H, Peisl J, Schittenhelm P and Abstreiter G 1999 *Appl. Phys. Lett.* **74** 2978–80
[49] Hosemann R and Bagchi S N 1962 *Direct Analysis of Diffraction by Matter* (*Series in Physics*) (Amsterdam: North-Holland)
[50] Castro M, Cuerno R, Vazquez L and Gago R 2005 *Phys. Rev. Lett.* **94** 016102
[51] Ziegler J, Biersack J P and Littmark U 1985 *The Stopping and Range of Ions in Solids* (New York: Pergamon)
[52] Keller A, Biermanns A, Carbone D, Grenzer J, Facsko S, Plantevin O, Gago R and Metzger T H 2009 *Appl. Phys. Lett.* submitted
[53] Carbone D, Plantevin O, Gago R A, Facsko S and Metzger T H, in preparation
[54] Hazra S, Chini T K, Sanyal M K, Grenzer J and Pietsch U 2004 *Phys. Rev.* B **70** 121307
[55] Biermanns A, Pietsch U, Grenzer J, Hanisch A, Facsko S, Carbone G and Metzger T H 2008 *J. Appl. Phys.* **104** 044312–5
[56] Grigorian S, Pietsch U, Grenzer J, Datta D P, Chini T K, Hazra S and Sanyal M K 2006 *Appl. Phys. Lett.* **89** 231915
[57] Robinson I K and Tweet D J 1992 *Rep. Prog. Phys.* **55** 599–651
[58] Thurn-Albrecht T, Zontone F, Grübel G, Steffen W, Müller-Buschbaum P and Patkowski A 2003 *Phys. Rev.* E **68** 031407
[59] Bikondoa O *et al*, in preparation
[60] Frömsdorf A, Kornowski A, Pütter S, Stillrich H and Lee L-T 2007 *Small* **3** 880–9